

# Efficient Oxidative Decomposition of Jet-Fuel *exo*-Tetrahydrodicyclopentadiene (JP-10) by Aluminum Nanoparticles in a Catalytic Microreactor: An Online Vacuum Ultraviolet Photoionization Study

Souvick Biswas, Dababrata Paul, Nureshan Dias, Wenchao Lu, Musahid Ahmed,\* Michelle L. Pantoya,\* and Ralf I. Kaiser\*



Cite This: *J. Phys. Chem. A* 2024, 128, 1665–1684



Read Online

ACCESS |



Metrics & More

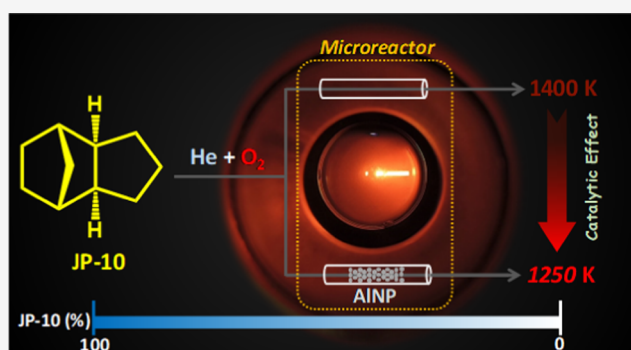


Article Recommendations



Supporting Information

**ABSTRACT:** The oxidation of gas-phase *exo*-tetrahydrodicyclopentadiene (JP-10, C<sub>10</sub>H<sub>16</sub>) over aluminum nanoparticles (AlNP) has been explored between a temperature range of 300 and 1250 K with a novel chemical microreactor. The results are compared with those obtained from chemical microreactor studies of helium-seeded JP-10 and of helium–oxygen-seeded JP-10 without AlNP to gauge the effects of molecular oxygen and AlNP, respectively. Vacuum ultraviolet (VUV) photoionization mass spectrometry reveals that oxidative decomposition of JP-10 in the presence of AlNP is lowered by 350 and 200 K with and without AlNP, respectively, in comparison with pyrolysis of the fuel. Overall, 63 nascent gas-phase products are identified through photoionization efficiency (PIE) curves; these can be categorized as oxygenated molecules and their radicals as well as closed-shell hydrocarbons along with hydrocarbon radicals. Quantitative branching ratios of the products reveal diminishing yields of oxidized species and enhanced branching ratios of hydrocarbon species with the increase in temperature. While in the low-temperature regime (300–1000 K), AlNP solely acts as an efficient heat transfer medium, in the higher-temperature regime (1000–1250 K), chemical reactivity is triggered, facilitating the primary decomposition of the parent JP-10 molecule. This enhanced reactivity of AlNP could plausibly be linked to the exposed reactive surface of the aluminum (Al) core generated upon the rupture of the alumina shell material above the melting point of the metal (Al).



## 1. INTRODUCTION

Jet Propellant-10 or JP-10 (*exo*-tetrahydrodicyclopentadiene, C<sub>10</sub>H<sub>16</sub>) represents a widely used hydrocarbon jet fuel with attractive properties such as high thermal stability, high density (0.94 g cm<sup>-3</sup>), low freezing point (194 K), and low flash point (327 K); this hydrocarbon also possesses a high volumetric energy density (39.6 kJ cm<sup>-3</sup>) originating from the inherent ring strain energy caused by three five-membered ring moieties incorporated into a single molecule.<sup>1,2</sup> Prior to the actual oxidation (combustion) of the hydrocarbon fuel, the endothermic chemical decomposition pathways function as a heat sink; this feature is essential in the thermal management and maintenance of the structural integrity of propulsion systems.<sup>3,4</sup> Over the past few years, JP-10 has emerged as a well-suited fuel for missiles, pulse detonation engines, and ramjets;<sup>5,6</sup> it has been explored to understand the underlying combustion chemistry using shock tubes,<sup>7</sup> flow tubes,<sup>8–11</sup> and high-temperature chemical reactors,<sup>12–15</sup> along with reaction modeling.<sup>7,9,16,17</sup>

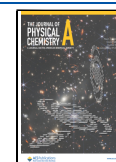
An effective approach to increase the energy density of the liquid hydrocarbon fuel is to include solid particle additives such as high energy-density nanoparticles (NPs).<sup>18,19</sup> In particular, metallic nanoparticle additives such as aluminum (84 kJ cm<sup>-3</sup>) have received significant attention for enhancing the performance of volume-limited propulsion systems, including JP-10.<sup>19,20</sup> Affordable aluminum nanoenergetic materials (ALNEM) offer key advantages such as a higher specific surface area, higher energy density, reduced ignition delays, and an enhanced heat transfer rate, which, in turn, improves the burning rates of liquid fuels via minimal fuel consumption, thereby influencing the emission characteristics of liquid fuels.<sup>20–31</sup>

**Received:** December 13, 2023

**Revised:** January 16, 2024

**Accepted:** January 30, 2024

**Published:** February 22, 2024



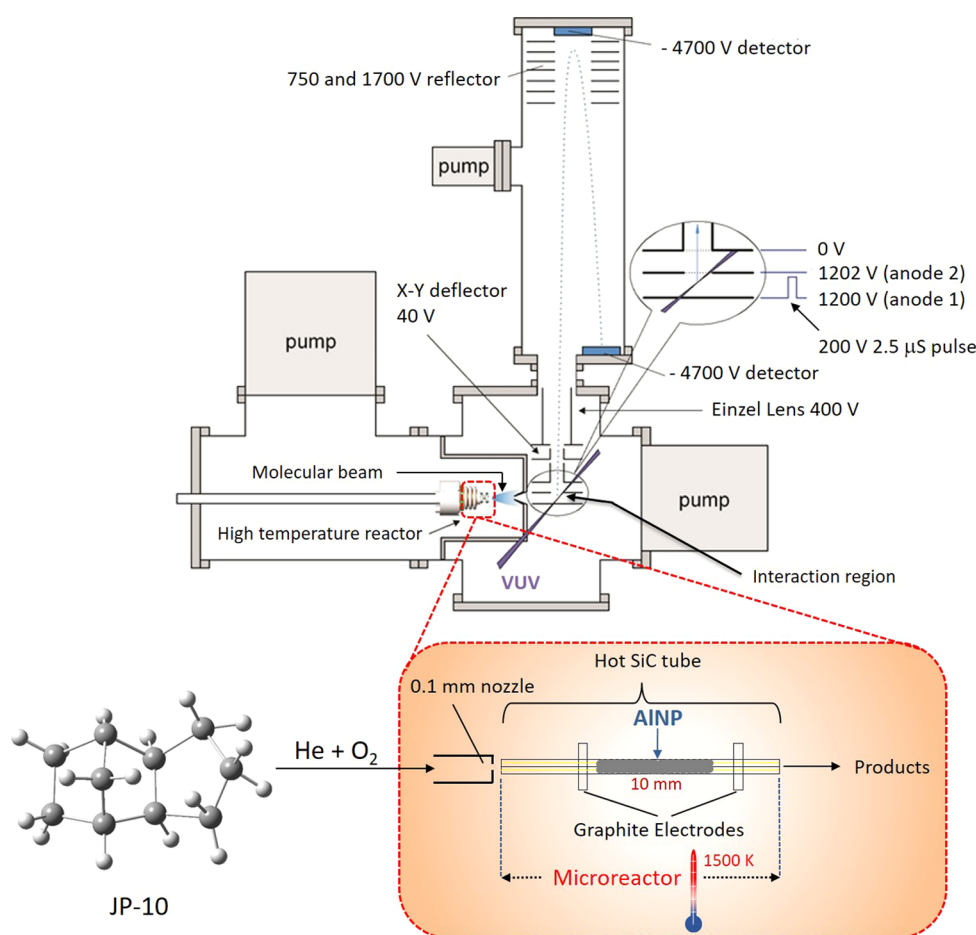


**Figure 1.** Schematics of the experimental setup including the high-temperature microreactor and reflectron time-of-flight mass spectrometer (ReTOF-MS). The mass spectrometer portion is adapted from ref-35 with permission from the Royal Society of Chemistry.<sup>35</sup>

An increase in the volumetric energy of JP-10 by 10% upon addition of 16 nm sized aluminum nanoparticles (AlNP) was reported;<sup>26,27</sup> ignition delay times were shortened with increased burn times in the combustion process in the temperature range of 1,500–1750 K. Luo et al. studied the combustion of JP-10 using a small-scale reactor containing 30–50 nm diameter AlNP, showing a higher combustion efficiency compared to pure JP-10 fuel.<sup>22</sup> Combustion studies of droplets of 80 nm diameter AlNP-doped JP-10 suspended on a silicon carbide (SiC) fiber were also performed by using a dedicated laser ignition system.<sup>24,25</sup> Combustion efficiency and engine performance were found to be enhanced remarkably by using JP-10 slurry fuel containing 16 wt % AlNP compared to pure JP-10 fuel in a scramjet engine.<sup>32</sup> As elucidated in the literature, the addition of AlNP also promoted the engine wall pressure along the combustor path to increase significantly. An impressive combustion efficiency of over 99% for the JP-10 droplet containing 10 wt % AlNP was reported by Chen et al.<sup>25</sup> Key studies from our laboratory explored the complex ignition and combustion chemistry of acoustically levitated AlNP-doped JP-10 droplets using a focused carbon dioxide (CO<sub>2</sub>) laser beam in an oxygen–argon mixture within a pressure-compatible process chamber interfaced to complementary Raman, ultraviolet–visible (UV–vis), and Fourier transform infrared (FTIR) spectroscopic probes.<sup>29–31</sup> Additionally, high-speed optical and infrared (IR) thermal imaging cameras were employed to monitor physical changes. The effects of untreated, prestressed, and superquenched aluminum particles

with different sizes and acetonitrile-milled aluminum particles on the combustion of JP-10 were also addressed, and a high combustion temperature of nearly 2600 K was noted.<sup>31</sup> As the major reactive intermediates, diatomic radicals such as hydroxyl (OH), methylidyne (CH), dicarbon (C<sub>2</sub>), and aluminum monoxide (AlO) were identified during the oxidation.<sup>30,31</sup>

Despite these prior studies on the combustion of AlNP/JP-10 mixed fuel, a complete understanding of the role of AlNP at the molecular level has not been revealed to date. Although offline and ex situ detection tools such as high-performance liquid chromatography (HPLC) and gas chromatography–mass spectrometry (GC–MS) are capable of identifying closed-shell products, short-lived reaction intermediates cannot be probed by these methods. These reactive transients, such as radicals formed in the initial stages of decomposition and oxidation, deliver the building blocks for the oxidation of JP-10 and hence control the overall efficiency and performance. Additionally, the lack of a comprehensive inventory of temperature-dependent products and intermediates restricts a proper understanding of the underlying chemistry of such fuel additives, influencing the combustion properties of JP-10. Therefore, in the present study, we exploit an isomer-selective in situ diagnostics study utilizing photoionization to probe the reaction products in a molecular beam at temperatures ranging from 300 to 1400 K. This approach utilizes the power of soft photoionization with single-photon synchrotron vacuum ultraviolet (VUV) light followed by a mass spectroscopic

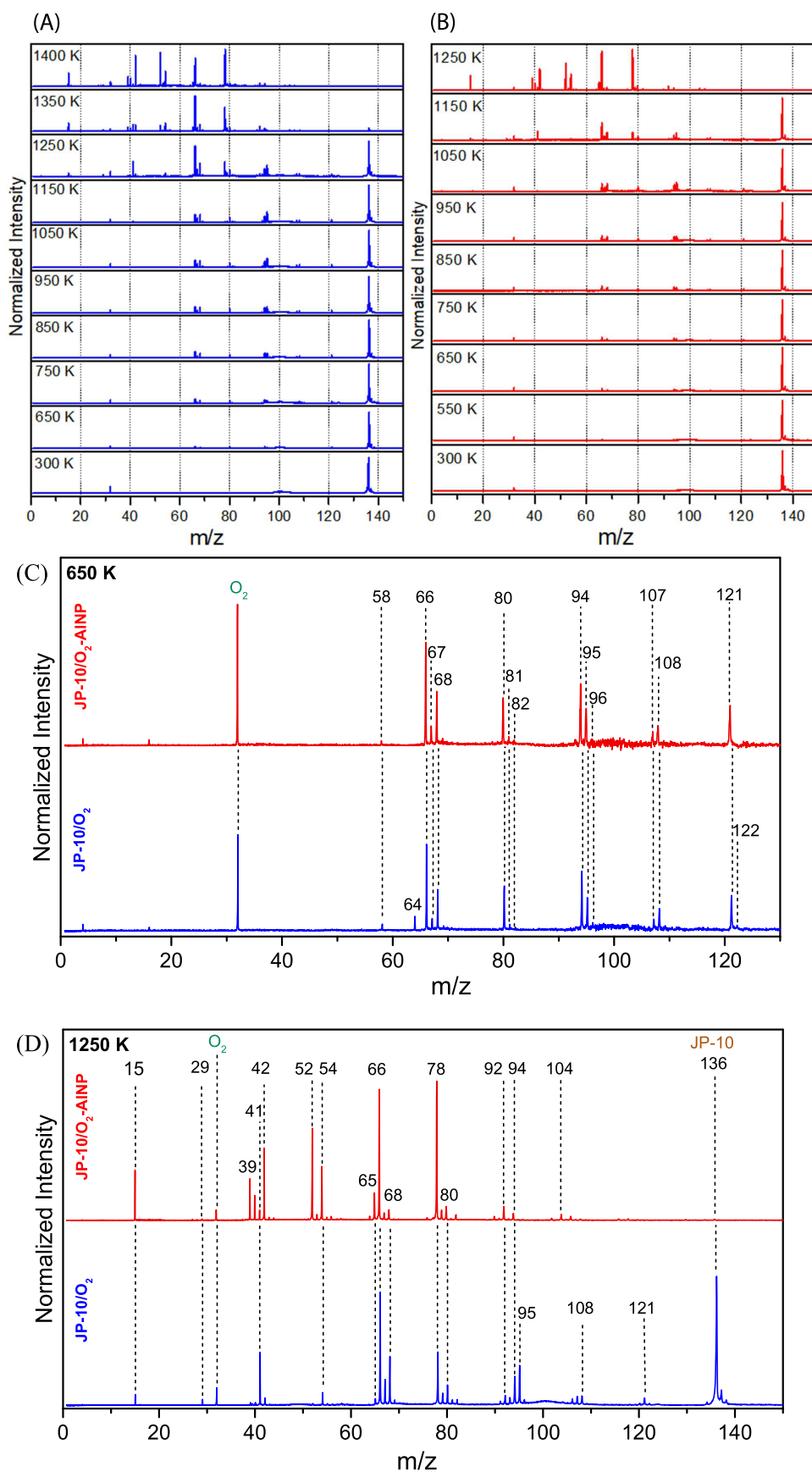


**Figure 2.** Mass spectra of products formed upon oxidation of JP-10 recorded at a photon energy of 10.0 eV in the 300–1400 K temperature range (A) without and (B) with the aluminum nanoparticles (AlNP) inside the high-temperature chemical microreactor (hot silicon carbide (SiC) tube). Simultaneous comparisons of the two cases with respect to the product peaks at two different temperatures (C) 650 K and (D) 1250 K are also presented.

analysis of the ions in a reflectron time-of-flight mass spectrometer (Re-TOF-MS).<sup>15,33,34</sup> The molecular beam was prepared by seeding JP-10 vapor in a helium (He)–oxygen (O<sub>2</sub>) gas mixture at an 80 to 20% volume ratio and passing this mixture over AlNP within a chemical microreactor (Figure 1). To elucidate the effects of the AlNP, the high-temperature oxidation of pure JP-10 was also conducted as a reference system within the same reactor at identical conditions but without the presence of AlNP. The experimental approach was validated by exploring the thermal cracking of JP-10 fuel through the chemical microreactor without the presence of any additive.<sup>15</sup> In the study mentioned above, 43 products were quantitatively identified, including alkenes, dienes, cumulenes, alkynes, enynes, diynes, cycloalkenes, cycloalkadienes, aromatic molecules, as well as short-lived open-shell species, such as ethyl (C<sub>2</sub>H<sub>5</sub>), allyl (C<sub>3</sub>H<sub>5</sub>), and methyl (CH<sub>3</sub>). Stable molecules detected were molecular hydrogen (H<sub>2</sub>), ethylene (C<sub>2</sub>H<sub>4</sub>), propene (C<sub>3</sub>H<sub>6</sub>), cyclopentadiene (C<sub>5</sub>H<sub>6</sub>), cyclopentene (C<sub>5</sub>H<sub>8</sub>), fulvene (C<sub>6</sub>H<sub>6</sub>), and benzene (C<sub>6</sub>H<sub>6</sub>). The present work also evaluates the temperature-dependent branching ratios of the products. This information is critical to developing predictive combustion models for nanoparticle-doped fuels and, ultimately to developing the next generation of air-breathing ramjet and scramjet systems with superior energy per unit volume and molecular weight compared to traditional hydrocarbon fuels such as JP-10.

## 2. EXPERIMENTAL METHODS

The thermal decomposition of JP-10 over AlNP was explored at the Chemical Dynamics Beamline (9.0.2.) of the Advanced Light Source (ALS) utilizing a high-temperature catalytic microreactor<sup>15,33,34</sup> (Figure 1). Briefly, the high-temperature microreactor consists of a resistively heated silicon carbide (SiC) tube of a 20 mm length and a 1 mm inner diameter, which was tightly packed with 80 nm sized aluminum nanoparticles (AlNP) over a length of 10 mm centered inside the SiC tube supported by a glass-wool bed (see the extended description and characterization of this reactor in Supporting Information, S1). Here, a helium (He; Airgas; 99.999%)–oxygen (O<sub>2</sub>; Matheson; 99.999%) mixture at (80:20) ± 1 at a backing pressure of 500 Torr passed through JP-10 (*exo*-tetrahydrodicyclopentadiene, C<sub>10</sub>H<sub>16</sub>) (TCI America; 94%) with a vapor pressure of 0.2 Torr<sup>1</sup> kept in a stainless-steel bubbler at room temperature (298 K). The gas mixture containing ~0.04% of JP-10 was introduced into the silicon carbide tube filled with the AlNP at temperatures from 300 to 1400 ± 10 K monitored by a type-C thermocouple. After exiting the reactor, the supersonic molecular beam, which contained the pyrolysis and oxidation products, passed a skimmer and entered the detection chamber, which housed the Wiley–McLaren reflectron time-of-flight mass spectrometer (Re-TOF-MS). The nascent products consisting of radicals and thermally labile closed-shell species were photoionized in the extraction region of the spectrometer by exploiting quasi-continuous tunable vacuum ultraviolet (VUV) light and detected with a microchannel plate (MCP) detector. Mass spectra were recorded in 0.05 eV intervals from 8.00 to 11.50 eV. This experiment was repeated under three conditions: the presence of pure He to simulate the pyrolysis condition, a mixture of He and O<sub>2</sub> to simulate the oxidation condition, and the presence of AlNP to simulate the catalytic conditions.

A set of additional mass spectra was also measured at 15.4 eV to photoionize molecular hydrogen and methane with

ionization energies of 15.4 and 12.6 eV, respectively. The PIE curves, which report the intensity of a selected mass-to-charge ratio (*m/z*) versus the photon energy, were extracted by integrating the signal collected at a specific *m/z* selected for the species of interest over the range of photon energies in 0.05 eV increases and normalized to the incident photon flux. The PIE curves were then fit with a linear combination of known PIE curves to isomer selectively identify the products.<sup>36</sup>

## 3. RESULTS

**3.1. Mass Spectra.** Characteristic mass spectra recorded during the oxidative decomposition of pure JP-10 (136 amu) without the presence of any additive at a photon energy of 10.0 eV are compiled in Figure 2(A) for distinct temperatures from 300 to 1400 K. Figure 2(B) compiles mass spectra when the JP-10 vapor seeded in a He–O<sub>2</sub> mixture was allowed to pass over AlNP inside the reactor. To compare the appearances of the products at a particular temperature, the mass spectra with and without the nanoparticles are also represented in Figure 2(C,D) recorded at distinct temperatures of 650 and 1250 K, respectively. The photon energy was purposefully chosen to be 10.0 eV while recording the photoionization mass spectra in order to avoid the formation of fragment ions from dissociative photoionization of JP-10 at photon energies above 10.0 eV, as shown in our previous publication.<sup>15</sup> At 300 K, for both the mass spectra (Figure 2A,2B) depicting only four peaks, the most intense one belongs to the molecular parent ion at *m/z* = 136 (C<sub>10</sub>H<sub>16</sub><sup>+</sup>) along with its weak <sup>13</sup>C counterpart at *m/z* = 137 (<sup>13</sup>CC<sub>9</sub>H<sub>16</sub><sup>+</sup>). The trace amount of higher harmonic VUV light photoionizes molecular oxygen (O<sub>2</sub>) and helium (He), resulting in the peaks at *m/z* = 32 (weak) and *m/z* = 4 (very weak), respectively. Upon gradually increasing the temperature of the microreactor and recording the corresponding mass spectra, product formation can be noted at 650 K for the oxidation of pure JP-10, indicating the commencement of decomposition for the fuel. At this temperature, apart from the mass peaks from reactant molecular oxygen (*m/z* = 32), helium (*m/z* = 4), and parent JP-10 ions (*m/z* = 136, 137), 16 additional *m/z* values at *m/z* = 58, 64, 66, 67, 68, 80, 81, 82, 93, 94, 95, 96, 107, 108, 121, and 122 were detected. However, in the presence of AlNP, the oxidative decomposition of JP-10 has been found to commence at 550 K, which is 100 K lower than without AlNP; this is accompanied by 12 product peaks (*m/z* = 58, 66, 67, 68, 80, 81, 94, 95, 96, 107, 108, and 121). It is worth mentioning that for the pyrolysis of pure JP-10, the thermally decomposed products started to form at a much higher temperature, i.e., at 1200 K.<sup>15</sup>

With an increase in the temperature, the number of mass peaks increased with and without AlNP (Figure 2). The temperature of the microreactor was increased to a point where the parent JP-10 ion peak completely vanished, implying its full decomposition. The presence of AlNP inside the reactor resulted in a significant lowering of the full decomposition temperature for JP-10 by 150 K compared to its oxidation without the additive and by 350 K with respect to its gas-phase thermal cracking.<sup>15</sup> During the oxidation in the absence of AlNP, it yielded 41 product mass peaks at the highest temperature (1400 K) and no survival of JP-10, whereas the same number of peaks emerged in the AlNP-assisted oxidation at its characteristic temperature of 1250 K. The features in the respective mass spectra representing the full decomposition of JP-10 with (1250 K) and without AlNP (1400 K) in the He–O<sub>2</sub> mixed carrier gas are similar, but the relative intensities of

the peaks are different. In general, the most intense mass peaks appear at  $m/z = 15, 39, 42, 52, 54, 66,$  and  $78$ . Even at high temperatures, no signal was observed at  $m/z$  values exceeding  $136$  ( $C_{10}H_{16}^+$ ) and  $137$  ( $^{13}CC_9H_{16}^+$ ); this finding rules out any molecular mass growth processes, representing the sensitive and crucial detection of the nascent decomposition and/or oxidation products of individual JP-10 molecules under our experimental conditions.

**3.2. Decomposition Profiles.** The most notable phenomenon derived from the above-mentioned mass spectra is the diminishing intensity for the parent molecular peak of JP-10 at  $m/z = 136$  ( $C_{10}H_{16}^+$ ) with increasing temperature. The intensity ratios of the decomposed peak at  $m/z = 136$  at the corresponding temperature to that of the intact JP-10 at 10 eV ionization energy are defined as the decomposition ratio (D.R.). Figure 3 depicts the plot of decomposition ratios as a

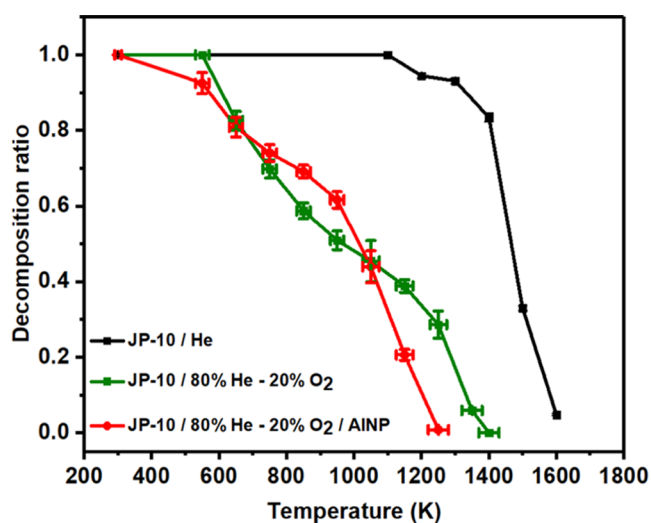


**Figure 3.** Decomposition ratios for JP-10 passing through the high-temperature chemical microreactor seeded in helium (black), a helium–oxygen mixture (green), and a helium–oxygen mixture over aluminum nanoparticles (AlNP) (red).

function of temperature for three different sets of reaction conditions: (i) pyrolysis (black trace; carrier gas: helium), (ii) oxidation (green trace; carrier gas: helium–oxygen mixture), and (iii) oxidation in the presence of AlNP (red trace; carrier gas: helium–oxygen mixture) of JP-10. The overall pattern for the decomposition ratio curves undergoing oxidations is remarkably distinct from the pyrolysis; the oxidation also results in a significantly earlier onset of decomposition of JP-10 at 550 K (red curve, with AlNP) and 650 K (green curve, without AlNP), respectively, compared to 1200 K for the pyrolysis (black curve), under otherwise identical experimental conditions.<sup>15</sup> The efficiency for the full decomposition of the JP-10 fuel was also enhanced for the oxidation processes compared to the pyrolysis; specifically, the oxidation in the presence of AlNP is found to be the most efficient among all of the mentioned cases (at 1250 K).

Based on the slope of the decomposition curves as a function of temperature for the oxidation processes, there are two temperature ranges: (i) the low-temperature region (550–1000 K) and (ii) the high-temperature region (1000–1400 K); a common trend is that the slope of the latter is much steeper than the former. Although the decomposition initiated at a lower temperature for the oxidation in the presence of AlNP,

the corresponding graph descends with a less steep slope (D.R. = 0.62 at 950 K) in the low-temperature segment compared to the oxidation in the absence of AlNP (D.R. = 0.51 at 950 K). However, above 1000 K, in the high-temperature region, the decomposition curve representing the oxidation in the presence of AlNP displays a sharp decline in the magnitudes of the decomposition ratios in comparison with that without any additive. This observation indicates the significant role of AlNP during the decomposition of the fuel, thus lowering the full decomposition temperature drastically.

**3.3. Identification of the Products: Photoionization Efficiency Curves.** To decipher the effects of oxidation of JP-10 with and without AlNP, the primary requisite is to identify the nature of the products entrained in the molecular beam. This is achieved through an extraction and detailed analysis of distinct PIE curves followed by a comparison with the products corresponding to the pure JP-10 pyrolysis.<sup>15</sup> Overall, 63 products were identified in each of the oxidation events,<sup>36–46</sup> which are constituted of four major classes: (i) oxidized molecules, (ii) oxidized radicals, (iii) closed-shell hydrocarbons, and (iv) hydrocarbon radicals. Table 1 provides an overview of these molecular classes, including their ionization energies and appearance temperature range. Figures 4, 5 and 6 display the PIE curve fittings for the identified species. The PIE curve fittings for the products from the oxidation of JP-10 without the nanoparticles are also shown in the Supporting Information, (Figures S2–S4). Table S1 represents a comparison of the appearance of the products generated in different experimental conditions: pyrolysis only, pyrolysis in the presence of AlNP, oxidation without any additive, and oxidation with AlNP.

The class of **oxidized molecules** formed includes aliphatic alcohols, ketones, and aldehydes, as well as cyclic (aromatic) alcohols, ketones, aldehydes, and ether. Initially, at relatively low temperature (650 K) for both the oxidation reactions, the major oxidized compounds (Figure 4 and Table 1) detected are furan ( $C_4H_4O$ ), 2,4-cyclopentadiene-1-one ( $C_5H_4O$ ), phenol ( $C_6H_5OH$ ), 2-cyclohexene-1-one ( $C_6H_8O$ ), cresol ( $CH_3C_6H_4OH$ ), benzyl alcohol ( $C_6H_5CH_2OH$ ), and dimethylphenol ( $(CH_3)_2C_6H_3OH$ ). The small-sized molecules (1–3 carbons) such as formaldehyde (HCHO), acetaldehyde ( $CH_3CHO$ ), ethenol ( $CH_2=CHOH$ ), and 2-propenal ( $CH_2=CHCHO$ ) tend to form at higher temperatures. Water (IE = 12.6 eV),<sup>47</sup> a common combustion end product, was also identified in the mass spectra recorded at 15.4 eV (Figure S5). At the initial decomposition temperature (650 K), larger open-shell **oxygenated radicals** (e.g., phenoxy ( $C_6H_5O^*$ ), methylphenoxy ( $CH_3C_6H_4O^*$ ), dimethylphenoxy ( $(CH_3)_2C_6H_3O^*$ ), etc.) have also been observed to form in addition to the oxidized molecules.<sup>43,45,46</sup> As the temperature increases to and surpasses 1,050 K, small-sized short-lived radicals like formyl ( $HCO^*$ ) and ethynoxy ( $HCCO^*$ ) radicals are also seen (Figure 4 and Table 1).

Various **closed-shell hydrocarbon molecules** were produced in the form of 1,3-cyclopentadiene ( $C_5H_6$ ), cyclopentene ( $C_5H_8$ ), cyclohexadiene ( $C_6H_8$ ), and cyclohexene ( $C_6H_{10}$ ) at the beginning of the oxidation process, at 650 K. As the temperature was increased, particularly at the corresponding decomposition temperatures of 1250 or 1400 K, a complex pool of closed-shell hydrocarbons was also discovered. The detected hydrocarbons are summarized in Table 1, and the PIE curve fittings for these molecules are shown in Figure 5. Many of these hydrocarbons were also detected in the decomposition

Table 1. Mass, Molecular Formula, Structure, and Ionization Energy (I.E.) of the Individual Products Formed during the Oxidation of JP-10 on AlNP<sup>a</sup>

Mass	Molecular formula	Name	Structure	I.E. (eV)	Temperature range of appearance
<i>Oxidized Molecules</i>					
18	H <sub>2</sub> O	Water		12.6	850 – 1,250 K
30	HCHO	Formaldehyde		10.9	1,250 K
44	C <sub>2</sub> H <sub>4</sub> O	Ethanol		9.3	1,250 K
		Acetaldehyde		10.2	1,250 K
56	C <sub>3</sub> H <sub>4</sub> O	2-Propenal		10.1	1,250 K
58	C <sub>3</sub> H <sub>6</sub> O	Acetone		9.7	550 – 1,250 K
		Propanal		9.9	550 – 1,250 K
		Propen-2-ol		8.6	550 – 1,250 K
68	C <sub>4</sub> H <sub>4</sub> O	Furan		8.8	550 – 1,250 K
80	C <sub>5</sub> H <sub>4</sub> O	2,4-Cyclopentadiene-1-one		9.4	550 – 1,250 K
82	C <sub>5</sub> H <sub>6</sub> O	2-Cyclopenten-1-one		9.4	550 – 1,250 K
94	C <sub>6</sub> H <sub>6</sub> O	Phenol		8.5	550 – 1,250 K
96	C <sub>6</sub> H <sub>8</sub> O	2-Cyclohexene-1-one		9.2	550 – 1,250 K
106	C <sub>7</sub> H <sub>6</sub> O	Benzaldehyde		9.5	1,050 – 1,250 K
108	C <sub>7</sub> H <sub>8</sub> O	Cresol		8.3	550 – 1,250 K
		Benzyl alcohol		9.0	550 – 1,250 K
122	C <sub>8</sub> H <sub>10</sub> O	Dimethylphenol		8.2	550 – 1,250 K
<i>Oxidized Radicals</i>					
29	CHO	Formyl		8.1	1,050 – 1,250 K
41	C <sub>2</sub> HO	Ethynyloxy		9.5	1,050 – 1,250 K
93	C <sub>6</sub> H <sub>5</sub> O	Phenoxy		8.6	550 – 1,250 K
95	C <sub>6</sub> H <sub>7</sub> O	1,3-Cyclohexadienyloxy		9.0	550 – 1,250 K
107	C <sub>7</sub> H <sub>7</sub> O	Methylphenoxy		8.5	550 – 1,250 K

Table 1. continued

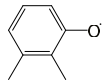
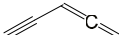
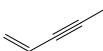
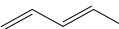
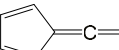
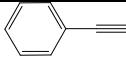
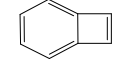
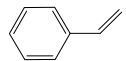
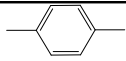
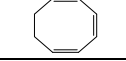
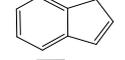
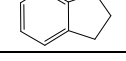
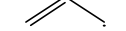
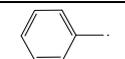
121	C <sub>8</sub> H <sub>9</sub> O	Dimethylphenoxy		8.4	550 – 1,250 K
<i>Hydrocarbon Molecules</i>					
16	CH <sub>4</sub>	Methane	CH <sub>4</sub>	12.6	1,250 K
26	C <sub>2</sub> H <sub>2</sub>	Acetylene	CH≡CH	11.4	1,250 K
28	C <sub>2</sub> H <sub>4</sub>	Ethylene	H <sub>2</sub> C=CH <sub>2</sub>	10.5	850 – 1,250 K
40	C <sub>3</sub> H <sub>4</sub>	Allene	H <sub>2</sub> C=C=CH <sub>2</sub>	9.7	1,250 K
		Methylacetylene		10.4	1,250 K
42	C <sub>3</sub> H <sub>6</sub>	Propene		9.7	1,250 K
50	C <sub>4</sub> H <sub>2</sub>	Diacetylene		10.1	1,250 K
52	C <sub>4</sub> H <sub>4</sub>	Vinylacetylene		9.6	1,250 K
54	C <sub>4</sub> H <sub>6</sub>	1,3-Butadiene		9.1	1,050 – 1,250 K
56	C <sub>4</sub> H <sub>8</sub>	1-Butene		9.6	1,250 K
		2-Butene		9.1	1,250 K
64	C <sub>5</sub> H <sub>4</sub>	Ethynylallene		9.2	1,250 K
66	C <sub>5</sub> H <sub>6</sub>	1,3-Cyclopentadiene		8.5	650 – 1,250 K
		1-Penten-3-yne		9.0	650 – 1,250 K
68	C <sub>5</sub> H <sub>8</sub>	Cyclopentene		9.0	650 – 1,250 K
		1,3-Pentadiene		8.6	650 – 1,250 K
76	C <sub>6</sub> H <sub>4</sub>	<i>o</i> -Benzyne		9.1	1,050 – 1,250 K
78	C <sub>6</sub> H <sub>6</sub>	Benzene		9.2	850 – 1,250 K
		Fulvene		8.4	850 – 1,250 K
80	C <sub>6</sub> H <sub>8</sub>	1,3-Cyclohexadiene		8.3	650 – 1,250 K
		1,4-Cyclohexadiene		8.8	650 – 1,250 K
82	C <sub>6</sub> H <sub>10</sub>	Cyclohexene		8.9	650 – 1,250 K
		2,4-Hexadiene		8.2	650 – 1,250 K
90	C <sub>7</sub> H <sub>6</sub>	Fulvenallene		8.3	1,250 K
92	C <sub>7</sub> H <sub>8</sub>	Toluene		8.8	650 – 1,250 K
		5-Methylene-1,3-cyclohexadiene		7.9	650 – 1,250 K

Table 1. continued

102	C <sub>8</sub> H <sub>6</sub>	Phenylacetylene		8.8	1,250 K
		Benzo[1,2-c]cyclobutene		7.5	1,250 K
104	C <sub>8</sub> H <sub>8</sub>	Styrene		8.4	850 – 1,250 K
106	C <sub>8</sub> H <sub>10</sub>	<i>p</i> -Xylene		8.5	1,050 – 1,250 K
		1,3,5-Cyclooctatriene		7.9	1,050 – 1,250 K
116	C <sub>9</sub> H <sub>8</sub>	Indene		8.3	1,050 – 1,250 K
		1-Ethynyl-4-methylbenzene		8.5	1,050 – 1,250 K
118	C <sub>9</sub> H <sub>10</sub>	Indane		8.5	1,050 – 1,250 K
<b>Hydrocarbon Radicals</b>					
15	CH <sub>3</sub>	Methyl	CH <sub>3</sub> <sup>•</sup>	9.8	1,250 K
27	C <sub>2</sub> H <sub>3</sub>	Vinyl	H <sub>2</sub> C=ĊH	8.3	1,250 K
29	C <sub>2</sub> H <sub>5</sub>	Ethyl	H <sub>3</sub> C-ĊH <sub>2</sub>	8.1	1,050 – 1,250 K
39	C <sub>3</sub> H <sub>3</sub>	Propargyl		8.7	1,250 K
41	C <sub>3</sub> H <sub>5</sub>	Allyl		8.1	1,050 – 1,250 K
65	C <sub>5</sub> H <sub>5</sub>	Cyclopentadienyl		8.4	1,050 – 1,250 K
91	C <sub>7</sub> H <sub>7</sub>	Benzyl		7.2	1,250 K

<sup>a</sup>The products are classified into different categories, and their temperature ranges of appearance are also compiled.

of helium-seeded JP-10<sup>15</sup> but only at temperatures exceeding 1200 K. In this study, a highly reactive organic hydrocarbon—*ortho*-benzyne (C<sub>6</sub>H<sub>4</sub>, *m/z* = 76) has also been detected at the full decomposition temperatures. The formation of isomeric species at *m/z* = 76, such as (*E*) and/or (*Z*)-hexa-1,5-diyne-3-ene (IE = 9.1 eV) could not be ruled out completely, but *o*-benzyne is likely to be the predominant or sole contributor as realized through the detection of a benzyl radical (C<sub>7</sub>H<sub>7</sub>, *m/z* = 91), which is a combination product of *o*-benzyne and a methyl radical.<sup>48</sup> For *m/z* = 80, the cyclohexadienes could have formed via the cyclization of the metastable, isomeric methylcyclopentadienes (IE = 8.4 eV).<sup>49</sup> The latter can also undergo endoergic rearrangement, followed by hydrogen loss, to produce fulvene at higher temperatures, which is identified above 850 K in this experiment.

On the other hand, none of the oxidation cases in the given temperature range resulted in the detection of the typical hydrocarbon decomposition product, the molecular hydrogen (H<sub>2</sub>), in the mass spectra recorded at an energy of 15.4 eV (Figure S5). Extraction of PIE curves further reveals that hydrocarbon radicals form in noticeable concentrations at temperatures exceeding 1,050 K as a general trend. These radicals are summarized in Table 1 and the corresponding PIE curve fittings are depicted in Figure 6. Among the observed species, the benzyl radical (C<sub>7</sub>H<sub>7</sub>) was exclusively detected in this study, and it was not reported in the pyrolysis study of helium-seeded JP-10.<sup>15</sup> The remaining weak mass peaks at *m/z*

= 53, 55, 67, 69, 79, and 81 have been assigned to the <sup>13</sup>C variant of some of the observed species by extracting and matching corresponding PIE curves with their <sup>12</sup>C analogues presented here, which are the major isotopic contributors (Figure S6).

**3.4. Temperature-Dependent Abundances.** 3.4.1. *Oxidized Products.* Figure 7 shows the normalized intensities as a function of the temperature for the mass peaks containing the oxidized products. The majority of the mass peaks (*m/z* = 93, 94, 95, 96, 107, 108, 121, 122) follow bell-shaped temperature-dependent yields with maxima observable in the temperature range of 1050 ± 100 K for both the oxidation processes, irrespective of the presence of AlNP. These species containing six and seven carbon atoms include oxygenated radicals carrying the (hydrogenated) benzene ring such as phenoxy (C<sub>6</sub>H<sub>5</sub>O<sup>•</sup>, *m/z* = 93), 1,3-cyclohexadienyloxy (C<sub>6</sub>H<sub>7</sub>O<sup>•</sup>, *m/z* = 95), methylphenoxy (C<sub>7</sub>H<sub>7</sub>O<sup>•</sup>, *m/z* = 107), and dimethylphenoxy radicals (C<sub>8</sub>H<sub>9</sub>O<sup>•</sup>, *m/z* = 121) along with phenol (C<sub>6</sub>H<sub>5</sub>OH, *m/z* = 94), 2-cyclohexene-1-one (C<sub>6</sub>H<sub>8</sub>O, *m/z* = 96), cresol (CH<sub>3</sub>C<sub>6</sub>H<sub>4</sub>OH, *m/z* = 108), benzyl alcohol (HOCH<sub>2</sub>C<sub>6</sub>H<sub>5</sub>, *m/z* = 108), and dimethylphenol ((CH<sub>3</sub>)<sub>2</sub>C<sub>6</sub>H<sub>3</sub>OH, *m/z* = 122). For these species, above 1050 K, the oxidation of JP-10 with AlNP is sharper than the one without the nanoparticles.

Each of the mass peaks for *m/z* = 29, 41, 56, 68, 80, 82, and 106 consists of multiple molecule(s) and/or radical(s). Their temperature-dependent abundances also display a complex

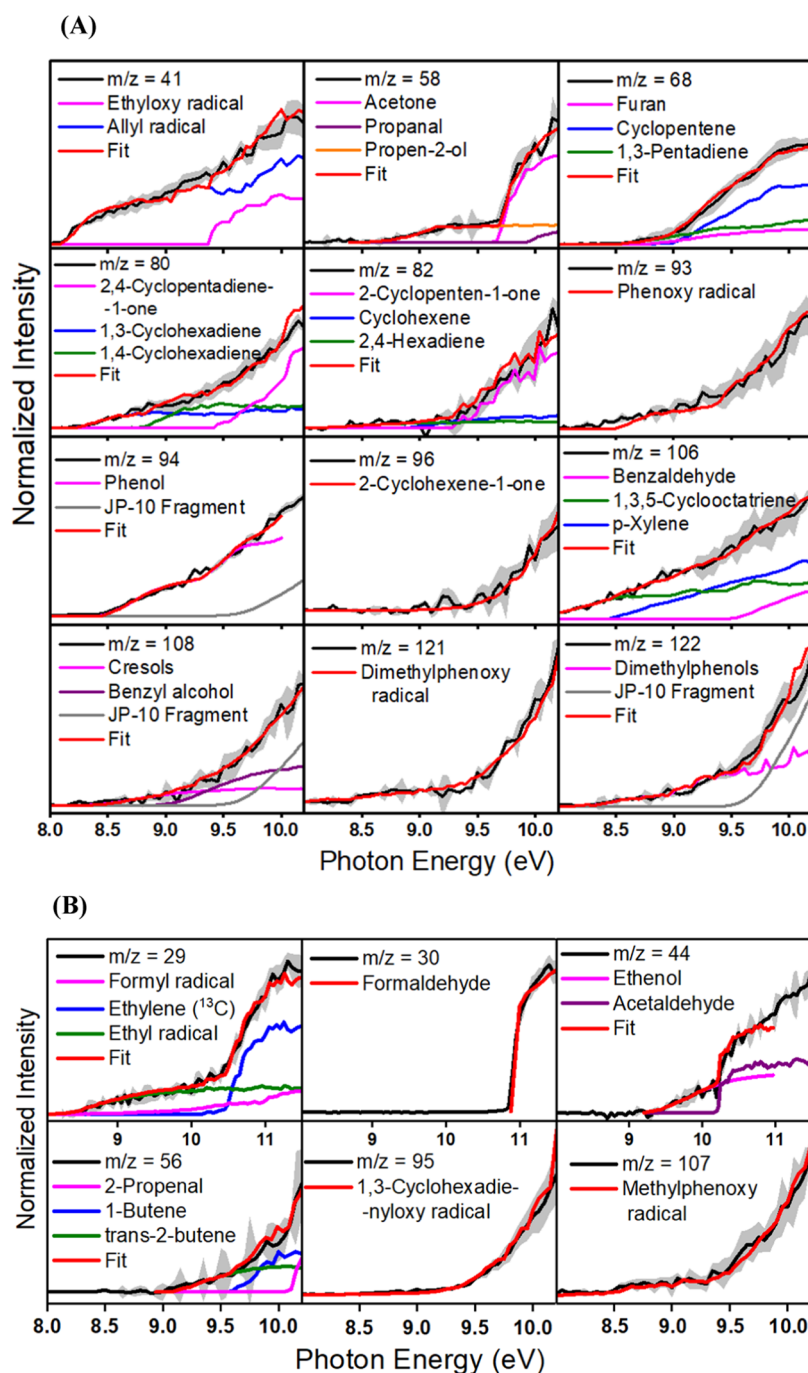


**Figure 4.** Experimental photoionization efficiency curves (PIE, black traces) for the oxidized products (magenta, purple, and orange reference traces) formed by the oxidation of JP-10 over aluminum nanoparticles (AINP) along with the experimental errors (gray shaded area). The errors originate from the measurement errors of the photocurrent by the photodiode and a  $1\sigma$  error of the PIE curves averaged over the individual scans. In the case of multiple isomeric contributions, individual reference PIE curves are presented, and the overall fitted curve is depicted by the red trace; the single-component fits are also shown with a red trace only. The JP-10 fragment implies the photolysis fragment of JP-10 generated upon dissociative photoionization.

pattern in general, having intensity maxima at around 1250 K followed by decay at higher temperatures for oxidation without the nanoparticles. In the presence of AINP, no decay for these peak intensities has been observed in the experimental heating temperature range of 650–1250 K, except for the  $m/z = 68$ , 80, and 82 peaks.

Considering the remaining mass peaks that correspond solely to the oxygenated species,  $m/z = 30$  (formaldehyde, HCHO),  $m/z = 44$  (acetaldehyde,  $\text{CH}_3\text{CHO}$  and ethenol,

$\text{CH}_2=\text{CHOH}$ ), and  $m/z = 58$  (acetone,  $\text{CH}_3\text{COCH}_3$ ; propanal,  $\text{CH}_3\text{CH}_2\text{CHO}$  and propen-2-ol,  $\text{CH}_3\text{C}(\text{OH})=\text{CH}_2$ ), the maximum abundance at 1,250 K for the AINP-assisted oxidation is evident; a similar pattern is observed for  $m/z = 44$  undergoing oxidation without any AINP additive. However, the maximum intensity has been marked at 1,350 K for the  $m/z = 30$ , 58 peaks in the latter case, and an overall diminished intensity for all of these three mass peaks is

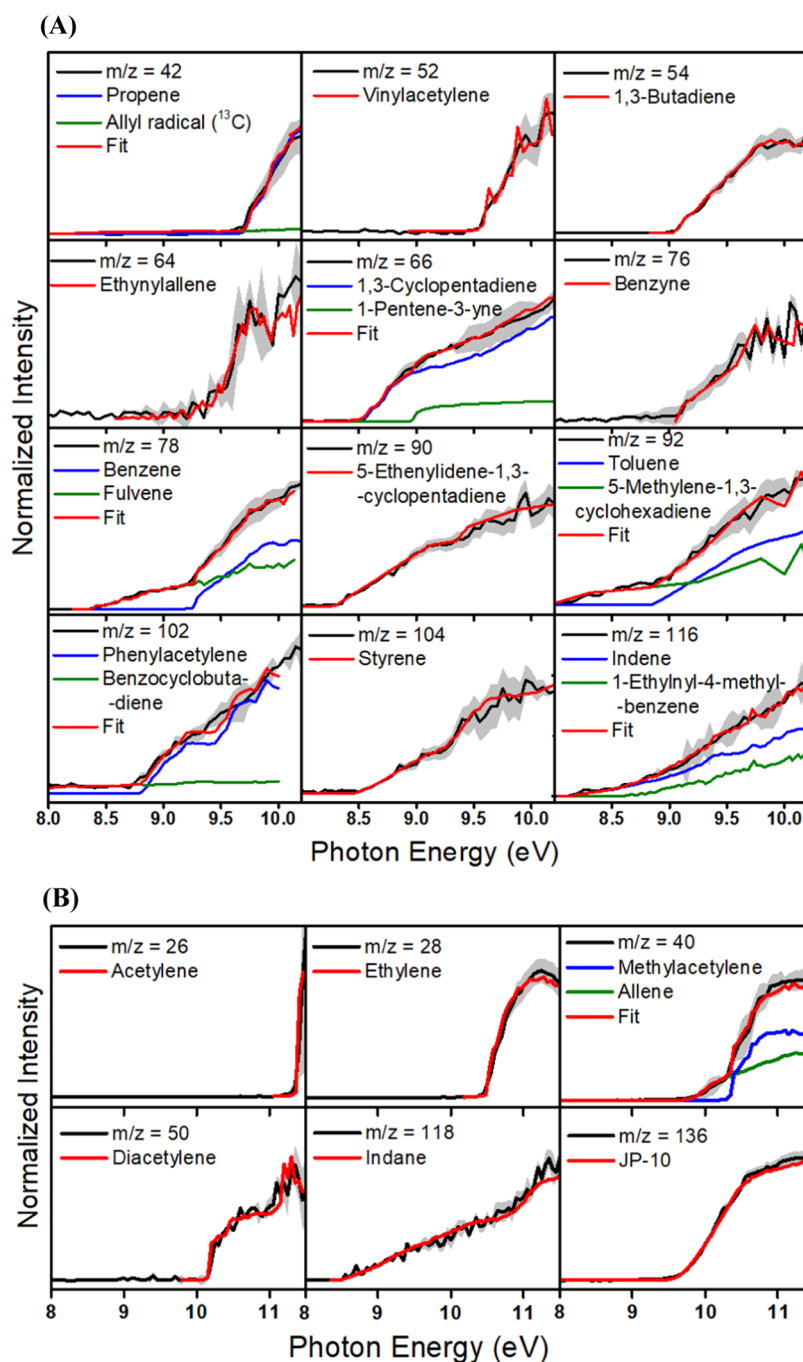


**Figure 5.** Experimental photoionization efficiency curves (PIE, black traces) in the range of (A) 8.0–10.2 eV and (B) 8.0–11.5 eV for the closed-shell hydrocarbon products (blue and green reference traces) generated during the oxidative decomposition of JP-10 over aluminum nanoparticles (AlNP) along with the experimental errors (gray shaded area). The errors originate from the measurement errors of the photocurrent by the photodiode and a  $1\sigma$  error of the PIE curves averaged over the individual scans. In the case of multiple isomeric contributions, individual reference PIE curves are presented, and the overall fitted curve is depicted by the red trace; the single component fits are also shown with a red trace only. The JP-10 fragment implies the photolysis fragment of JP-10 generated upon dissociative photoionization.

recorded at the maximum temperature during heating (1400 K).

**3.4.2. Hydrocarbon Radicals.** The trend in the temperature-dependent abundances of the hydrocarbon radicals [ $m/z = 15$  (methyl,  $\bullet\text{CH}_3$ ),  $m/z = 27$  (vinyl,  $\bullet\text{CH}=\text{CH}_2$ ),  $m/z = 39$  (propargyl,  $\bullet\text{CH}_2-\text{C}\equiv\text{CH}$ ),  $m/z = 65$  (cyclopentadienyl,  $\bullet\text{C}_5\text{H}_5$ ) and  $m/z = 91$  (benzyl,  $\bullet\text{C}_7\text{H}_7$ )] is significantly different from the oxidized products. The temperature versus intensity plots for hydrocarbon radicals are shown in Figure 8.

During the oxidation of JP-10 carried out without any additive, the generation of open-shell hydrocarbon products has been registered to begin from 1250 K, except for the vinyl radical ( $m/z = 27$ ), which could be detected at and above 1350 K. Other than the benzyl radical ( $m/z = 91$ ), the abundances for all of the other radicals increased until the highest temperature of the experiment was reached (1400 K). In the presence of the AlNP, the formation of all of the mentioned hydrocarbon radicals in detectable amounts is found to

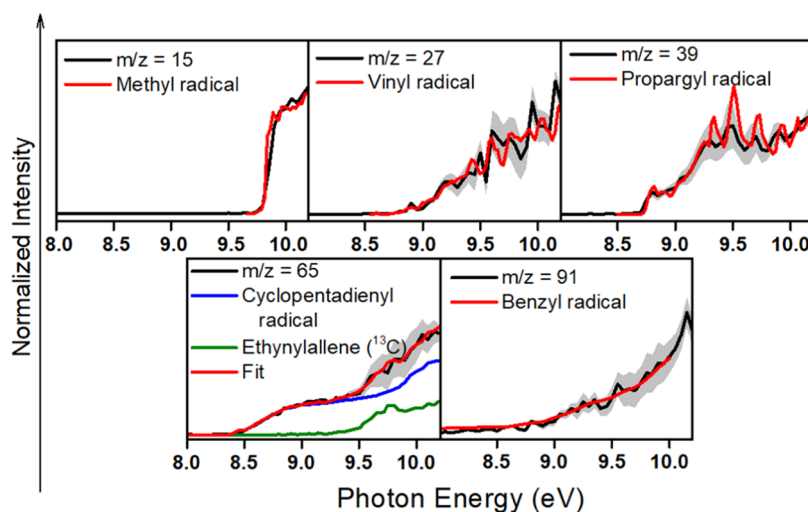


**Figure 6.** Experimental photoionization efficiency curves (PIE, black traces) for the hydrocarbon radical products formed during the oxidative decomposition of JP-10 over aluminum nanoparticles (AlNP) along with the experimental errors (gray shaded area) originating from the measurement errors of the photocurrent by the photodiode and a  $1-\sigma$  error of the PIE curves averaged over the individual scans. In the case of multiple isomeric contributions, individual reference PIE curves are presented, and the overall fitted curve is depicted by the red trace. The JP-10 fragment implies the photolysis fragment of JP-10 generated upon dissociative photoionization.

commence also at 1250 K, except for the benzyl radical ( $m/z = 91$ ), whose significant formation is initiated early, at 1150 K. It is notable that the temperature-dependent radical yields are remarkably shifted toward lower temperature during the oxidation in the presence of AlNP.

**3.4.3. Hydrocarbon Molecules.** The temperature evolution-normalized intensity plot for the hydrocarbon species observed in this study is depicted in Figure 9. The formation of closed-shell hydrocarbon species is favored at elevated temperatures. Among the aliphatic unsaturated hydrocarbons, except for the  $m/z = 54$  (1,3-butadiene,  $\text{H}_2\text{C} = \text{CH}-\text{CH} = \text{CH}_2$ ) and  $m/z = 56$  (1-butene,  $\text{H}_3\text{C}-\text{CH}_2-\text{CH} = \text{CH}_2$  and 2-butene,  $\text{H}_3\text{C}-\text{CH}_2-\text{CH} = \text{CH}_2$ ) peaks, the intensities of the rest tend to increase until the highest temperature (1400 K) for the oxidation without AlNP. Under similar experimental conditions, while formation of some of the cyclic hydrocarbons is facilitated [benzyne ( $\text{C}_6\text{H}_4$ ,  $m/z = 76$ ), 5-ethynylidene-1,3-cyclopentadiene/fulvenallene ( $\text{C}_7\text{H}_6$ ,  $m/z = 90$ ), phenylacetylene and benzocyclobutadiene ( $\text{C}_8\text{H}_6$ ,  $m/z = 102$ )], rest of the cyclic hydrocarbons have been observed to decline slightly with the increase in temperature. Generally, the extent of the decline in the mass peak intensities is greater for the larger hydrocarbons.

The presence of AlNP in the course of oxidative decomposition of JP-10 induces an early initiation for the generation of a few hydrocarbons compared to the oxidation without the nanoparticles, such as acetylene ( $m/z = 26$ ), ethylene ( $m/z = 28$ ), diacetylene ( $m/z = 50$ ), vinylacetylene ( $m/z = 52$ ), benzyne ( $m/z = 76$ ), fulvenallene ( $m/z = 90$ ), phenylacetylene/benzocyclobutene ( $m/z = 102$ ), and indene/1-ethynyl-4-methylbenzene ( $m/z = 116$ ). On an interesting note, the hydrocarbon molecules with a higher degree of unsaturation are set to form at much lower temperatures with AlNP; especially, the generation of *o*-benzyne at a temperature of 1050 K is remarkable.

**3.5. Product Branching Ratios.** In order to visualize the quantitative product distribution over the entire temperature range, the bar charts of the branching ratios of each product formed during the oxidation of JP-10 without and with AlNP

are shown in Figure 10 at different temperatures. The respective individual branching ratios are calculated by accounting for the photoionization cross sections.<sup>15</sup> Both the plots represent similar trends, but the remarkable dissimilarity belongs to the product distributions at 1250 K for the given oxidation parameters. However, the branching ratios for the products formed in the presence of AlNP at this temperature match closely with the oxidation products generated in the absence of AlNP at 1400 K.

The most prominent primary products formed at 650 K in the presence of AlNP are 1,3-cyclopentadiene ( $\text{C}_5\text{H}_6$ ,  $32.8 \pm 1.3\%$ ), methylphenoxy radical ( $(\text{CH}_3)\text{C}_6\text{H}_4\text{O}^\bullet$ ,  $12.9 \pm 1.1\%$ ), dimethylphenoxy radical ( $(\text{CH}_3)_2\text{C}_6\text{H}_3\text{O}^\bullet$ ,  $9.4 \pm 0.1\%$ ), 1,3-cyclohexadienyloxy radical ( $\text{C}_6\text{H}_7\text{O}^\bullet$ ,  $7.3 \pm 0.8\%$ ), 1-penten-3-yne ( $\text{C}_5\text{H}_6$ ,  $6.6 \pm 0.7\%$ ), phenol ( $\text{C}_6\text{H}_5\text{OH}$ ,  $4.8 \pm 0.1\%$ ), and 2,4-cyclopentadiene-1-one ( $\text{C}_5\text{H}_4\text{O}$ ,  $3.6 \pm 0.9\%$ ). The corresponding branching ratios of the above-mentioned products are also in the comparable range ( $\pm 1.0\%$ ) in the case of oxidation in absence of the AlNP, except slightly higher for 1,3-cyclopentadiene ( $36.3 \pm 1.3\%$ ) and dimethylphenoxy radical ( $11.2 \pm 0.9\%$ ). Remarkably, the primary difference relates to the phenoxy radical ( $\text{C}_6\text{H}_5\text{O}^\bullet$ ), which is only generated in the presence of AlNP at this temperature ( $4.6 \pm 0.1\%$ ).

The total branching ratios for the oxidized products versus hydrocarbons with and without AlNP are displayed in Figure 11. At 1050 K, the total yield of oxidized species ( $65.3 \pm 2.3\%$  with AlNP versus  $69.4 \pm 1.9\%$  without AlNP) exceeds the combined share of hydrocarbons and hydrocarbon radicals. Phenoxy ( $\text{C}_6\text{H}_5\text{O}^\bullet$ ), methylphenoxy ( $(\text{CH}_3)\text{C}_6\text{H}_4\text{O}^\bullet$ ), 1,3-cyclohexadienyloxy ( $\text{C}_6\text{H}_7\text{O}^\bullet$ ), and dimethylphenoxy radicals ( $(\text{CH}_3)_2\text{C}_6\text{H}_3\text{O}^\bullet$ ) along with 2-cyclohexene-1-one ( $\text{C}_6\text{H}_8\text{O}$ ), phenol ( $\text{C}_6\text{H}_5\text{OH}$ ), 2,4-cyclopentadiene-1-one ( $\text{C}_5\text{H}_4\text{O}$ ), benzyl alcohol ( $\text{C}_6\text{H}_5\text{CH}_2\text{OH}$ ), and furan ( $\text{C}_4\text{H}_4\text{O}$ ) emerge as the major oxidized products at this temperature. At 1250 K, the comparison between JP-10 oxidation with and without AlNP reveals notable distinctions. The presence of AlNP leads to reduced branching ratios for oxidized products while exhibiting higher values for specific unsaturated hydro-

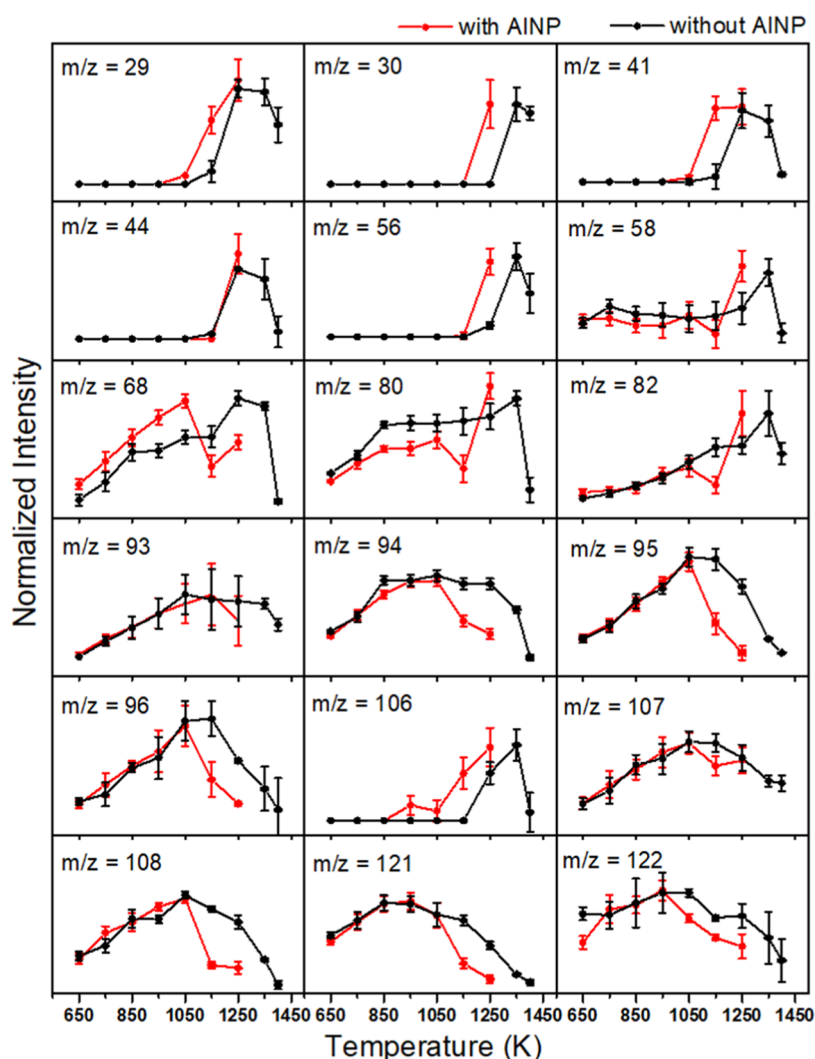


**Figure 7.** Comparison of temperature-dependent abundances of the mass peaks corresponding to oxidized products (as a function of normalized mass peak intensities) in presence (red trace) and absence (black trace) of AINP during oxidation of JP-10 in the temperature range of 650–1400 K. The  $y$ -error bars are due to the experimental errors of the mass peak intensities evaluated by averaging recorded mass spectra.

carbons/hydrocarbon radicals. The oxidized species are found to have lower individual shares in the overall product distribution for the AINP-assisted oxidation, as shown in Table 2. On the contrary, the production of hydrocarbon radicals and unsaturated hydrocarbons was clearly facilitated in the presence of AINP (Table 2), except in the case of the most contributing product—1,3-cyclopentadiene. At the higher temperatures, the small C1–C4 hydrocarbons also noticeably appear in both the oxidations, and the trend is identical to that seen in the case of pyrolysis of pure JP-10.

The general trend in both of the oxidation cases at their corresponding full decomposition temperature of JP-10 reveals the major products to be 1,3-cyclopentadiene ( $C_5H_6$ ), benzene ( $C_6H_6$ ), a cyclopentadienyl radical ( $\cdot C_5H_5$ ), toluene ( $C_7H_8$ ), 5-methylene-1,3-cyclohexadiene ( $C_7H_8$ ), styrene ( $C_7H_8$ ), 1-penten-3-yne ( $C_5H_6$ ), propene ( $C_3H_6$ ), and a methyl radical ( $\cdot CH_3$ ). Only two oxidized products, specifically the open-shell species phenoxy ( $C_6H_5O\cdot$ ) and methylphenoxy radicals ( $(CH_3)C_6H_4O\cdot$ ) are obtained with measurable branching ratios of about 2%.

#### 4. DISCUSSION

The above-mentioned observations suggest a complex chemistry involved in the oxidation of JP-10 compared to the simple pyrolytic cracking of the fuel studied earlier.<sup>15</sup> The presence of AINP during oxidation induces further critical effects. Multiple key outcomes from the experimental results can be extracted, which not only highlight the chemical transformations during the oxidative decomposition of JP-10 but also assess the significant role of the AINP in facilitating the oxidation process.

Notably, the presence of AINP lowers the onset temperature for oxidative decomposition by 100 K (550 K compared with 650 K without AINP). It is also worth mentioning that the initial product formation commenced at a significantly lower temperature than 1200 K, as reported for the thermal decomposition of the precursor.<sup>15</sup> Moreover, AINP-assisted oxidation achieves full fuel decomposition at 1250 K, much earlier compared to the oxidation without AINP (1400 K) and helium-seeded thermal decomposition at 1600 K. This indicates that AINP eases the oxidation process, allowing it to occur at a much lower temperature.

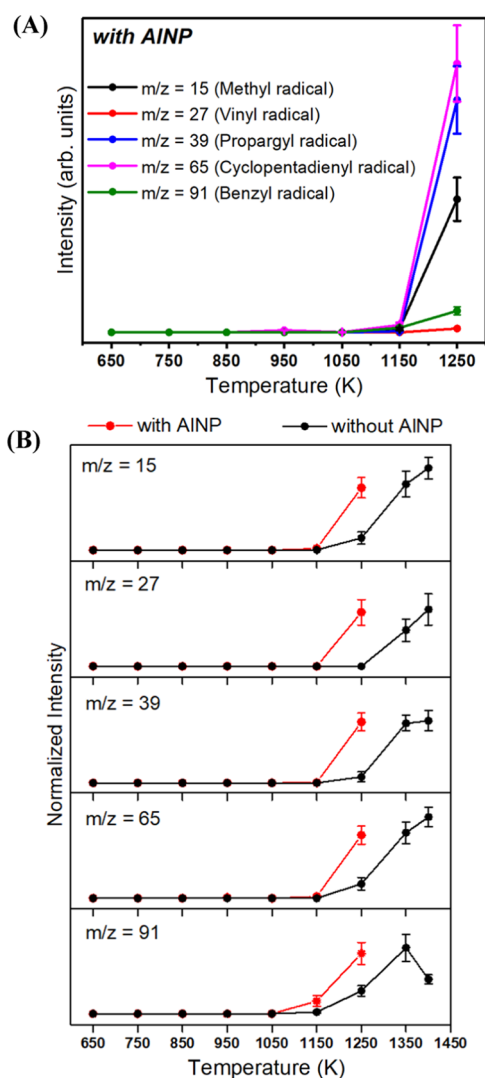


**Figure 8.** (A) Temperature-dependent abundances of hydrocarbon radicals in the presence of aluminum nanoparticles (AlNP) probed as a function of absolute intensity in the mass spectra and (B) comparison of the abundances (as a function of normalized mass peak intensities versus temperature) of hydrocarbon radicals in the presence (red trace) and the absence (black trace) of AlNP during oxidation of JP-10. The y-error bars are due to the experimental errors of the mass peak intensities evaluated by averaging recorded mass spectra.

In addition, the decomposition patterns of the fuel as a function of temperature during the oxidation and the pyrolysis are significantly distinct; especially, the oxidation with and without the AlNP represent mutually exclusive trends in the corresponding decomposition curves (Figure 3) with contrasting efficiencies in two temperature regimes: 550–1000 and 1000–1400 K.

At 650 K, the early oxidative decomposition stages of JP-10 lead to the detection of various five- and six-membered cyclic oxygenated molecules and radicals (Table 1). On the other hand, 1,3-cyclopentadiene dominates the yield among the five-membered cyclic hydrocarbons. In total, 23 oxidized products, including water, are formed (Figures 4–6 and 10).

The temperature-dependent abundances of the products in Figure 7 show a bell-shaped pattern for oxidized radicals and molecules, except for  $m/z = 29, 41, 56, 68, 80, 82,$  and 106,

indicating complex trends possibly involving multiple molecules and/or radicals. The overall branching ratios for the oxidized species reach a peak at 1050 K regardless of the presence of AlNP (Figure 11). However, in the JP-10/AlNP oxidation system, the temperature-dependent decay of these species is enhanced.

The open-shell hydrocarbon species cyclopentadienyl ( $C_5H_5^\bullet$ ), propargyl ( $C_3H_3^\bullet$ ), and methyl ( $CH_3^\bullet$ ) radicals are detected from  $1,050 \pm 100$  K onward and only significantly increase as the temperature increases until the full decomposition of JP-10 (Figures 2, 8, and 10). Particularly, for the vinyl and benzyl radicals, the onset temperature of formation is 100 K lowered through the presence of AlNP compared to that of the oxidation of JP-10 without the AlNP additive.

Finally, the yields of the closed-shell hydrocarbon molecules exceed those of the oxidation products at temperatures above 1200 K (Figure 11); as a common trend, the presence of AlNP lowers the temperature by 100 K for the initial production. The major contributors of the hydrocarbon molecules at the full decomposition temperatures are 1,3-cyclopentadiene ( $C_5H_6$ ), benzene ( $C_6H_6$ ), toluene ( $C_7H_8$ ), styrene ( $C_7H_8$ ), and propene ( $C_3H_6$ ); the detection of highly unsaturated hydrocarbons such as acetylene ( $C_2H_2$ ), allene ( $C_3H_4$ ), methylacetylene ( $C_3H_4$ ), diacetylene ( $C_4H_2$ ), vinylacetylene ( $C_4H_4$ ), ethynylallene ( $C_5H_4$ ), phenylacetylene ( $C_8H_6$ ), and reactive benzyne ( $C_6H_4$ ) is notable too.

Considering a general oxidation process of JP-10, mechanistic paths are proposed to involve an initial endoergic decomposition to  $C_{10}H_{15}$  radicals—either by atomic hydrogen losses operating in the pyrolysis of JP-10<sup>15</sup> or an atomic hydrogen (H) abstraction channel by molecular oxygen ( $O_2$ ). A schematic for the generation of early intermediates from JP-10 via the two possible pathways is shown simultaneously in Figure 12.

The analogy of the proposed formation of  $C_{10}H_{15}$  radicals with and without oxygen is experimentally implicated through the detection of ubiquitous five-membered cyclic hydrocarbons 1,3-cyclopentadiene ( $C_5H_6$ ) and cyclopentene ( $C_5H_8$ ) at the initial decomposition temperatures. From R1, these species could be formed with associated endoergies of 225 and 297  $\text{kJ mol}^{-1}$ , respectively.<sup>15</sup> However, the energetics of the elementary steps leading to the formation of in situ-generated JP-10 radicals ( $C_{10}H_{15}$ : R1–R6, Figure 12) reveal an endoergic requirement by  $\sim 200$   $\text{kJ mol}^{-1}$  on average in the case of the H-abstraction channel by molecular  $O_2$  as compared to that of  $\sim 400$   $\text{kJ mol}^{-1}$  for the homolytic C–H cleavage. This lowering of reaction enthalpies reflects on the early onset of decomposition of JP-10 at 650 K in the presence of molecular oxygen instead of 1200 K, as recorded for the pyrolysis event. Subsequently, the oxidation reactions may proceed via addition of molecular oxygen to the radical sites, followed by isomerization and/or fragmentation of reactive, oxygenated intermediates, yielding oxygenated as well as hydrocarbon species.

**4.1. Low-Temperature Regime.** Analyzing the trends in the low-temperature regime (550–1050 K) of the decomposition curves, it is apparent that although there is an earlier onset of product formation in the presence of AlNP, the overall decomposition efficiencies of up to 1000 K are slightly less than the oxidation in the absence of AlNP. This influence of the AlNP could have originated from the existing passivation layer of alumina ( $Al_2O_3$ ) surrounding the metallic core (Al).<sup>50–54</sup> It has been suggested that the release of the

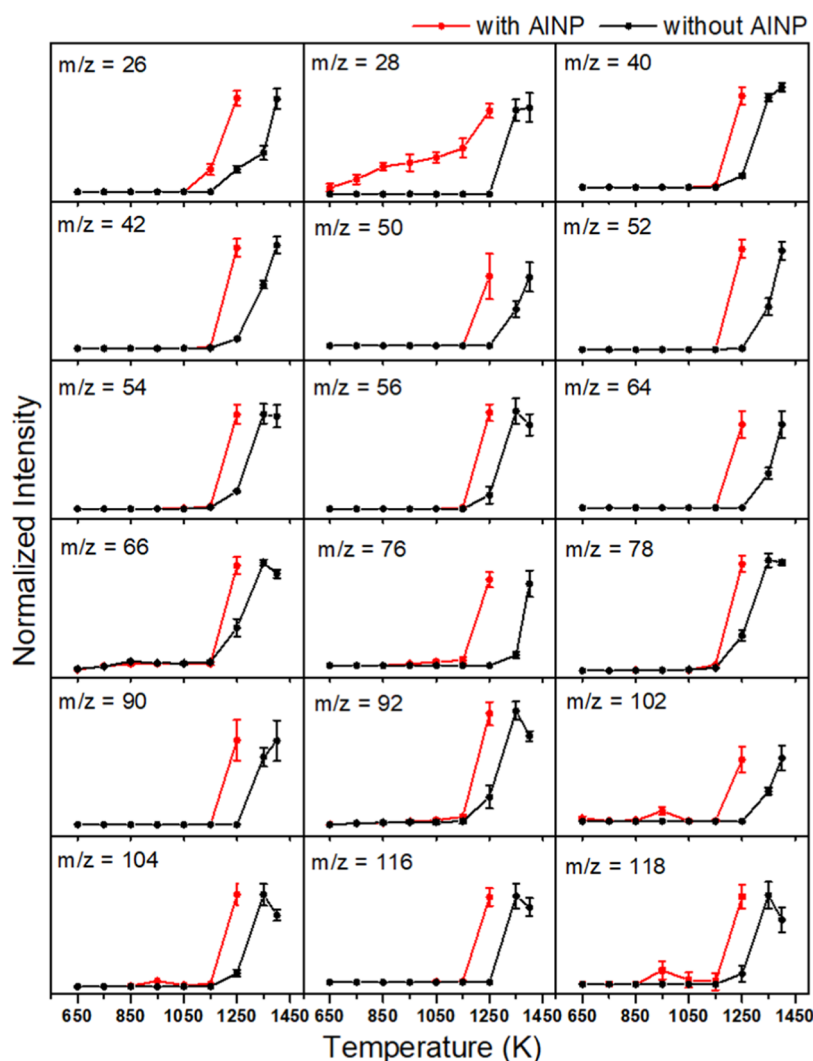


**Figure 9.** Comparison of temperature-dependent abundances of the mass peaks corresponding to closed-shell hydrocarbon products (as a function of normalized mass peak intensities) in presence (red trace) and absence (black trace) of AlNP during oxidation of JP-10. The y-error bars are due to the experimental errors of the mass peak intensities evaluated by averaging recorded mass spectra.

acquired chemical energy within the particle via diffusion-controlled chemical reactions is vastly hindered due to the  $\text{Al}_2\text{O}_3$  shell on the Al core, and the shell itself serves as a barrier. However, the aforementioned analogy is counter-intuitive according to the very recent findings that reveal unusual chemical reactivity of the alumina shell toward JP-10 during a thermal decomposition study in the absence of molecular oxygen.<sup>46</sup> Hence, the contrasting nature of the alumina layer, that is, the suppression of its reactivity in the present work, emerges owing to the presence of oxygen ( $\text{O}_2$ ) flow in the molecular beam. Due to the significant partial pressure of oxygen in the sample mixture and the inertness of the alumina coating, individual hot JP-10 molecules prefer interaction with gaseous oxygen molecules instead of the oxide layer on the nanoparticles. In addition, from a statistical viewpoint, the higher concentration of oxygen most likely obstructs the adsorption of the JP-10 molecules on the alumina surface of AlNP, thus restricting the heterogeneous oxygen-atom transfer step from the shell material to the JP-10 radicals ( $\text{C}_{10}\text{H}_{15}$ : R1–R6).<sup>46</sup> Previous experimental and computational studies also suggested that the oxide shell can grow and thicken and/or undergo phase change in an oxygen-rich environment

at elevated temperatures via the chemisorption of molecular oxygen on the partially oxidized sites and naked metallic surfaces,<sup>55–60</sup> this would constrain the chances of fuel–AlNP chemical interactions at this temperature regime. Summing up the above-mentioned factors, it can be concluded that in the low-temperature segment, AlNP does not exhibit any noticeable chemical activity, except being a better heat transfer medium, that is, by supplying about  $200 \text{ kJ mol}^{-1}$  energy (Figure 12) to the JP-10 +  $\text{O}_2$  reaction system, which allows the formation of a  $\text{C}_{10}\text{H}_{15}$  radical precursor and ultimately resulting in an early onset of decomposition.

**4.2. High-Temperature Regime.** At the higher-temperature end ( $\geq 1200 \text{ K}$ ), the yield of the hydrocarbon molecules and radicals exceeds that of the oxidized species; this corroborates that the endoergic ( $\sim 400 \text{ kJ mol}^{-1}$ ) pyrolysis channels of JP-10<sup>15</sup> (Figure 12) are accessible easily and preferred over the competing oxidation channels in this temperature regime. Moreover, the decline in the yields of the oxidized species as a function of temperature suggests that these molecules become thermally unstable, thus undergoing facile decomposition. This scenario is in line with the detection of small-sized (C1–C2) oxygenated species at elevated

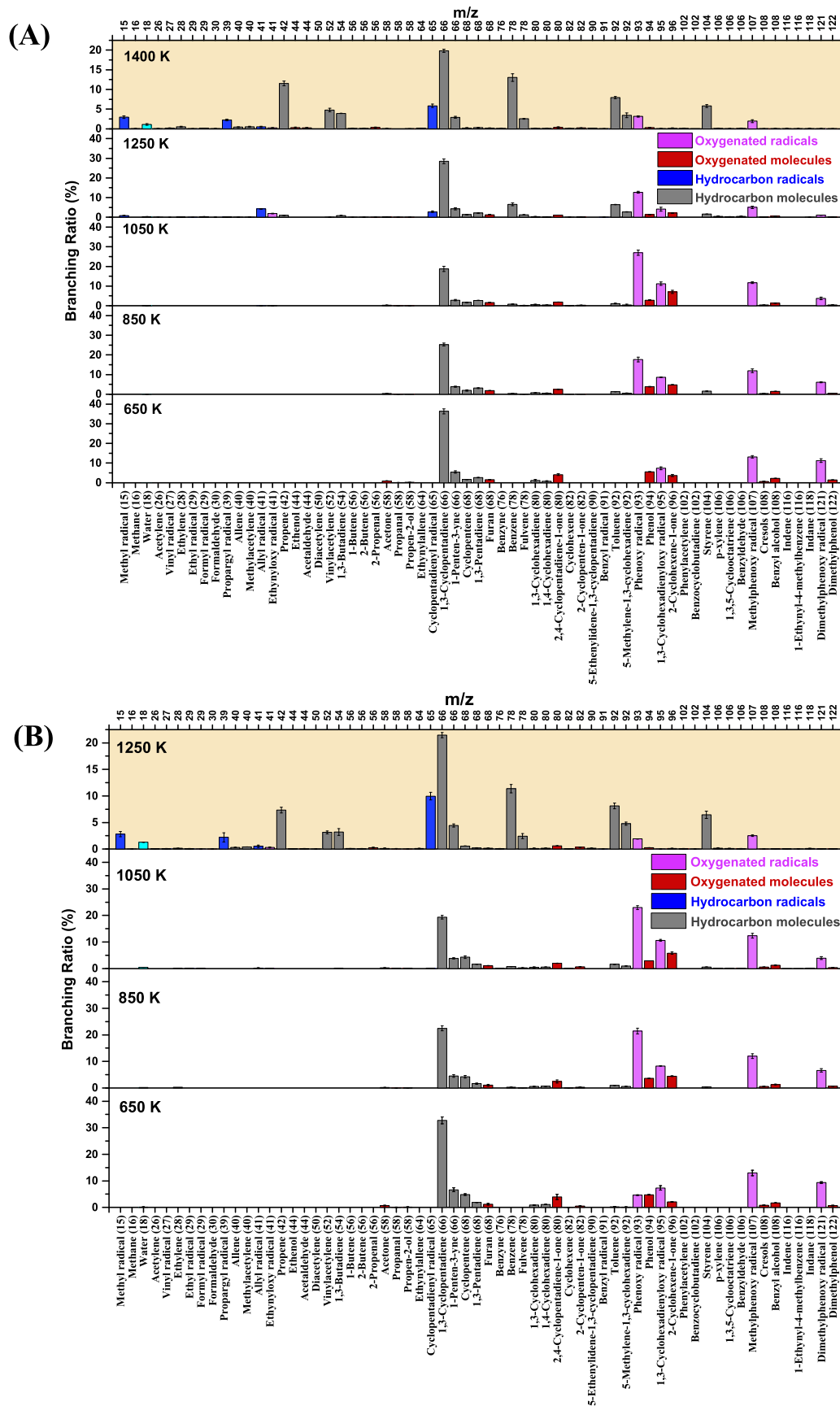


**Figure 10.** Individual branching ratios of the species obtained in the oxidative decomposition of JP-10 (A) in the absence of aluminum nanoparticles (AlNP) and (B) in the presence of AlNP for the temperature range (A) 650–1250 K and (B) 650–1400 K, respectively. The error bars are evolved due to the uncertainties determined by averaging the recorded photoionization efficiency curves. The topmost shaded areas at temperatures 1400 and 1250 K depict full decomposition of JP-10 in the absence and the presence of AlNP, respectively.

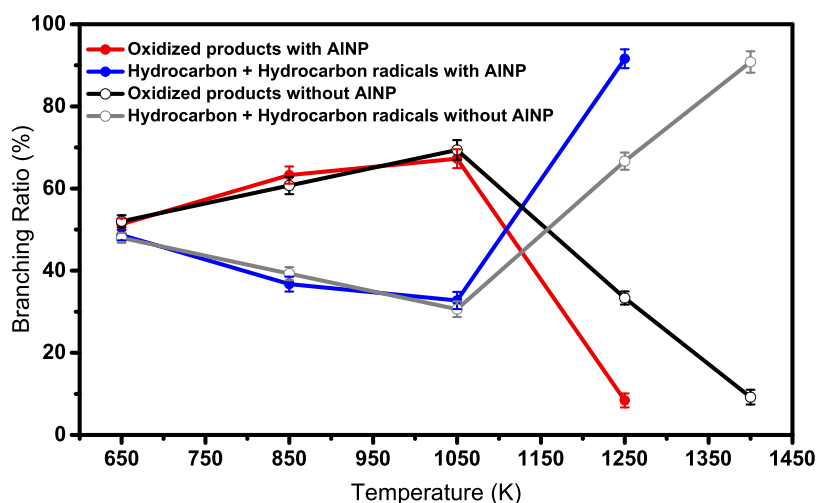


**Figure 11.** Overall branching ratios for the oxidized products versus hydrocarbon molecules and radicals collectively during oxidation of JP-10 in the presence of aluminum nanoparticles (AINP, blue and red traces) and in the absence of AINP (black and gray traces), respectively. The error bars are linked with the standard errors in the individual branching ratios.

**Table 2.** Branching Ratios of a Few Key Species at 1250 K for the Oxidation of JP-10 without and with AINP

species	molecular formula	branching ratio	
		Without AINP (%)	With AINP (%)
phenoxy radical	$C_6H_5O^\bullet$	$12.7 \pm 0.4$	$1.9 \pm 0.1$
phenol	$C_6H_5OH$	$1.4 \pm 0.1$	$0.3 \pm 0.1$
1,3-cyclohexadienyloxy radical	$C_6H_7O^\bullet$	$4.1 \pm 1.0$	$0.03 \pm 0.01$
methylphenoxy radical	$(CH_3)C_6H_4O^\bullet$	$5.1 \pm 0.6$	$2.5 \pm 0.1$
dimethylphenoxy radical	$(CH_3)_2C_6H_3O^\bullet$	$1.1 \pm 0.1$	$0.05 \pm 0.01$
methyl radical	$^\bullet CH_3$	$0.8 \pm 0.1$	$2.8 \pm 0.5$
propargyl radical	$^\bullet C_3H_3$	$0.2 \pm 0.1$	$2.2 \pm 0.8$
propene	$C_3H_6$	$0.9 \pm 0.1$	$7.4 \pm 0.5$
vinylacetylene	$H_2C=CH-C\equiv CH$	$0.05 \pm 0.01$	$3.1 \pm 0.3$
1,3-butadiene	$H_2C=CH-CH=CH_2$	$0.9 \pm 0.1$	$3.2 \pm 0.6$
cyclopentadienyl radical	$^\bullet C_5H_5$	$2.8 \pm 0.4$	$10.0 \pm 0.7$
benzene	$C_6H_6$	$6.6 \pm 0.7$	$11.4 \pm 0.8$
fulvene	$C_6H_6$	$1.2 \pm 0.1$	$2.4 \pm 0.4$
toluene	$C_7H_8$	$6.4 \pm 0.1$	$8.1 \pm 0.5$
styrene	$C_8H_8$	$1.6 \pm 0.1$	$6.5 \pm 0.7$
1,3-cyclopentadiene	$C_5H_6$	$28.5 \pm 1.1$	$21.5 \pm 0.5$

temperatures, such as the formyl radical (HCO), formaldehyde ( $H_2CO$ ), the ethynyloxy radical (HCCO), acetaldehyde ( $CH_3CHO$ ), and ethenol ( $C_2H_3OH$ ). The complicated pattern in the temperature-dependent abundance plot (Figure 7) for some multicomponent mass peaks could be explained by the combined effects of the thermal instabilities and corresponding yields for the constituent oxidized species as opposed to hydrocarbon radicals or/and molecules.

The presence of AINP in the microreactor further lowers the decomposition temperatures for JP-10 during the oxidation compared to the pyrolysis; this lowering might be linked to two effects mediated by AINP: (i) the large specific surface area-to-volume ratio for the nanoparticles can act as an excellent heat supplier with thermal conductivity of AINP at room temperature =  $237 \text{ W m}^{-1} \text{ K}^{-1}$ <sup>61</sup> during contact with the JP-10 vapor and may enhance the extent of thermal energy transfer to the parent molecule exceeding the predicted reaction enthalpies of  $+400 \text{ kJ mol}^{-1}$  for the initial C–H bond cleavage to occur at lower temperature and (ii) active chemistry of the AINP inducing a facile C–H bond cleavage.

As we move to the high-temperature range (1000–1400 K), the decomposition curve becomes much steeper in the presence of AINP; a full decomposition of the fuel is achieved at a much lower temperature of 1250 K; further, the generation of intermediate hydrocarbon radicals commenced much earlier compared to the oxidation in the absence of any additive (Figure 8) (1050 K). These crucial observations collectively suggest a strong chemical activity of the AINP. At temperatures above the melting point of the AINP (933 K), it is proposed that the alumina shell ruptures due to the volume expansion of the Al core, generating aluminum nanodroplets. These exposed nanodroplets<sup>62–66</sup> at the given temperature range react violently with the molecular oxygen, yielding reactive intermediates such as aluminum monoxide (AlO) and atomic oxygen ( $Al + O_2 \rightarrow AlO + O$ ),<sup>66</sup> both of which can facilitate the C–H bond cleavage of parent JP-10 molecules<sup>46</sup> compared to the oxidation without the additives and thus supply sufficient precursors (e.g., hydrocarbon radicals) for quantitative decomposition. The atomic oxygen-mediated pathways generating the initial  $C_{10}H_{15}$  radicals (R1–R6) plus the

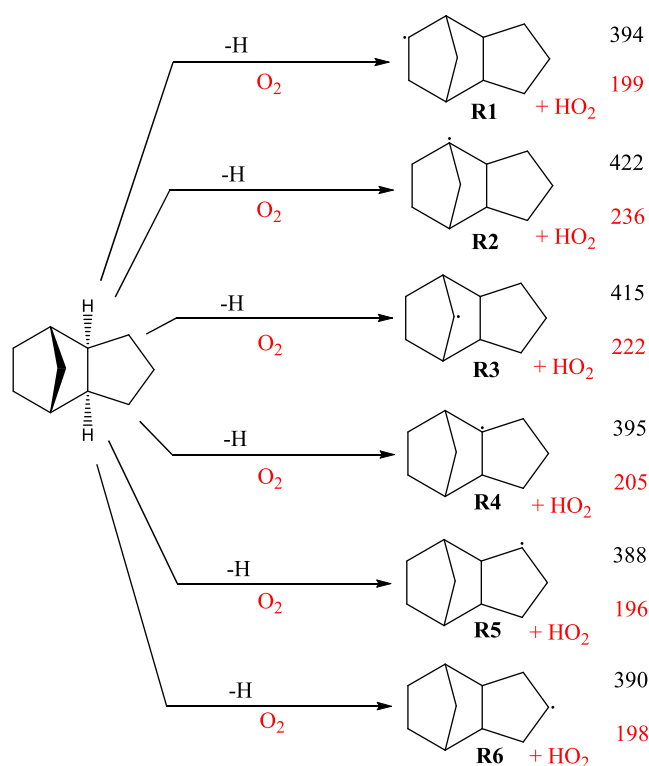


**Figure 12.** Schematic for the formation of initial intermediates from JP-10; hydrocarbon radicals ( $C_{10}H_{15}$ : R1–R6) upon pyrolytic C–H bond cleavages (above the arrow, black) and via the abstraction of atomic hydrogen by molecular oxygen (below the arrow, red) with the computed reaction enthalpies in  $\text{kJ mol}^{-1}$  at the B3LYP/6-311G\*\* level.<sup>15,30</sup> These radicals subsequently participate in the oxidation chemistry, leading to the formation of oxygenated species.

hydroxyl radical (OH) involve enthalpy changes in the range of  $-29$  to  $11 \text{ kJ mol}^{-1}$ . On the other hand, the aluminum monoxide (AlO)-driven H-atom abstraction pathways are predicted to be exoergic, spanning a range of  $-64$  to  $-24 \text{ kJ mol}^{-1}$ .<sup>30</sup> The energy barriers of  $4$ – $20 \text{ kJ mol}^{-1}$  from the separated reactants (JP-10 + AlO) can be spontaneously accessed at the given temperature range to produce van der Waal complexes between the  $C_{10}H_{15}$  radicals and AlOH, stabilized by  $-71$  to  $-109 \text{ kJ mol}^{-1}$  prior to the formation of separated products. Being a highly reactive intermediate, AlO is likely to get fully consumed within the reactor tube while readily reacting with the parent hydrocarbon molecule and finally dissipating in the molten aluminum matrix, leaving no traces of gaseous AlO to be detected. An earlier onset for the significant yields in the hydrocarbon radicals and molecules (Figures 8 and 9) also renders direct evidence in favor of the enhanced chemical reactivity exhibited by the AlNP. On the contrary, the accelerated decomposition of the oxidized species, i.e., representing the steeper slope in the temperature-dependent yield curves (Figure 7) in the presence of AlNP, in turn, supports the fact that at a high temperature, the exposed Al core surface should trigger their fragmentations. Nevertheless, besides possessing influential reactivity, these nanoparticles still may function as superior heat transfer media. Thus, the critical temperature lowering for the destruction of JP-10 could be attributed to an efficient catalytic effect of the AlNP, and slashing the decomposition temperature by  $100$ – $150 \text{ K}$  definitely provides an essential advantage for

implementing realistic next-generation engine designs in the air-breathing propulsion systems.

## 5. CONCLUSIONS

The oxidation of *exo*-tetrahydrodicyclopentadiene (JP-10,  $C_{10}H_{16}$ ) has been explored over a combustion-relevant temperature range of up to  $1400 \text{ K}$  in a chemical microreactor in the presence of aluminum nanoparticles (AlNP); the results are compared to those obtained from the oxidation of the fuel without AlNP additives under otherwise identical experimental conditions. The temperature-dependent product distributions are unambiguously identified by exploiting isomer-selective vacuum ultraviolet (VUV) photoionization mass spectrometry and extracting photoionization efficiency (PIE) curves. The mass spectra reveal an early onset of product formation at  $550 \text{ K}$  during oxidation in the presence of AlNP compared to the initial decomposition at  $1200 \text{ K}$  in the case of gas-phase pyrolysis of JP-10. The primary products consist of cyclic, oxidized species such as 2,4-cyclopentadiene-1-one ( $C_5H_4O$ ), phenol ( $C_6H_5OH$ ), 1,3-cyclohexadienyloxy radical ( $C_6H_7O^\bullet$ ), methylphenoxy radical ( $(CH_3)C_6H_4O^\bullet$ ), and dimethylphenoxy radical ( $(CH_3)_2C_6H_3O^\bullet$ ) along with the five-membered cyclic hydrocarbon, 1,3-cyclopentadiene ( $C_5H_6$ ). At the highest temperature, apart from the major cyclic hydrocarbon products, 1,3-cyclopentadiene ( $C_5H_6$ ), benzene ( $C_6H_6$ ), cyclopentadienyl radical ( $C_5H_5^\bullet$ ), and toluene ( $C_7H_8$ ), a few aliphatic species—1-penten-3-yne ( $C_5H_6$ ), propene ( $C_3H_6$ ), and methyl radical ( $CH_3^\bullet$ )—are also detected. The temperature-dependent decomposition curves of the parent JP-10 display a decrease in the decomposition temperature by  $100$ – $150 \text{ K}$  in the presence of AlNP, thus indicating the critical role of AlNP in the decomposition of JP-10. While the trend in the decomposition patterns for the oxidation processes and that of the pyrolysis are remarkably different, the curves for the oxidation with and without AlNP are also mutually exclusive in the low-temperature ( $300$ – $1000 \text{ K}$ ) and high-temperature ( $1000$ – $1400 \text{ K}$ ) ranges. As evaluated from the product branching ratios, in the low-temperature range, the oxidized molecules and radicals are found to be dominant products; with the increase in temperature, hydrocarbon molecules and radicals prevail. AlNP is suggested to act as efficient heat transfer media triggering the oxidative decomposition of JP-10,  $100 \text{ K}$  lower than the oxidation without the additive. At elevated temperatures ( $1000$ – $1400 \text{ K}$ ), the decomposition of JP-10 is significantly enhanced in the presence of AlNP and reveals quantitative destruction of the fuel at  $1250 \text{ K}$ . This efficient role of the AlNP likely emerged from the spallation of the reactive aluminum metallic core, which reacts with molecular oxygen, generating aluminum monoxide (AlO) and atomic oxygen followed by their chemical interactions through hydrogen atom abstraction from JP-10, easing the primary C–H cleavage compared to that in the gas phase, thus resulting into a remarkable lowering in the energy barrier. The detailed findings of this experimental study contribute to the development of next-generation air-breathing propulsion systems with aluminum nanoenergetic material (ALNEM)-assisted JP-10 combustions, thus maintaining lower operational engine temperatures, which provide higher sustainability and longer flight time.

## ■ ASSOCIATED CONTENT

### SI Supporting Information

The Supporting Information is available free of charge at <https://pubs.acs.org/doi/10.1021/acs.jpca.3c08125>.

Optimization of catalyst packing in SiC microreactors; photoionization efficiency curves for the oxidized products, hydrocarbon radicals, and closed-shell hydrocarbons during the oxidative decomposition of JP-10 without AlNPs; details of the observed products and their appearances in the oxidation of JP-10 with and without AlNPs along with the thermal decomposition of pure JP-10 and in the presence of AlNPs; mass spectra of the products formed upon oxidation of JP-10 with and without AlNPs recorded at a photon energy of 15.4 eV; and photoionization efficiency curves for the mass peaks having contribution(s) from  $^{13}\text{C}$  only species in the presence and the absence of AlNPs (PDF)

## ■ AUTHOR INFORMATION

### Corresponding Authors

**Musahid Ahmed** – Chemical Sciences Division, Lawrence Berkeley National Laboratory, Berkeley, California 94720, United States; [orcid.org/0000-0003-1216-673X](https://orcid.org/0000-0003-1216-673X); Email: [mahmed@lbl.gov](mailto:mahmed@lbl.gov)

**Michelle L. Pantoya** – Mechanical Engineering Department, Texas Tech University, Lubbock, Texas 79409, United States; [orcid.org/0000-0003-0299-1832](https://orcid.org/0000-0003-0299-1832); Email: [michelle.pantoya@ttu.edu](mailto:michelle.pantoya@ttu.edu)

**Ralf I. Kaiser** – Department of Chemistry, University of Hawai'i at Manoa, Honolulu, Hawaii 96822, United States; [orcid.org/0000-0002-7233-7206](https://orcid.org/0000-0002-7233-7206); Email: [ralfk@hawaii.edu](mailto:ralfk@hawaii.edu)

### Authors

**Souvick Biswas** – Department of Chemistry, University of Hawai'i at Manoa, Honolulu, Hawaii 96822, United States

**Dababrata Paul** – Department of Chemistry, University of Hawai'i at Manoa, Honolulu, Hawaii 96822, United States

**Nureshan Dias** – Chemical Sciences Division, Lawrence Berkeley National Laboratory, Berkeley, California 94720, United States

**Wenchao Lu** – Chemical Sciences Division, Lawrence Berkeley National Laboratory, Berkeley, California 94720, United States; [orcid.org/0000-0002-3798-5128](https://orcid.org/0000-0002-3798-5128)

Complete contact information is available at: <https://pubs.acs.org/10.1021/acs.jpca.3c08125>

### Notes

The authors declare no competing financial interest.

## ■ ACKNOWLEDGMENTS

The authors are thankful for support from the United States Office of Naval Research (ONR) under Contract Numbers N00014-22-1-2010 (Hawaii) and N00014-22-1-2006 (Texas). N.D., W.L., and M.A. are supported by the Director, Office of Science, Office of Basic Energy Sciences, of the U.S. Department of Energy under Contract No. DE-AC02-05CH11231, through the Gas Phase Chemical Physics Program of the Chemical Sciences Division. The Advanced Light Source at Berkeley is also supported under contract No. DE-AC02-05CH11231. The authors thank Dr. Oleg Kostko

for his valuable technical assistance at the Beamline 9.0.2 Advanced Light Source.

## ■ REFERENCES

- (1) Chung, H. S.; Chen, C. S. H.; Kremer, R. A.; Boulton, J. R.; Burdette, G. W. Recent Developments in High-Energy Density Liquid Hydrocarbon Fuels. *Energy Fuels* **1999**, *13*, 641–649.
- (2) Edwards, T. Liquid Fuels and Propellants for Aerospace Propulsion: 1903–2003. *J. Propul. Power* **2003**, *19*, 1089–1107.
- (3) Huang, H.; Spadaccini, L.; Sobel, D. In *Endothermic Heat-Sink of Jet Fuels for Scramjet Cooling*, 38th AIAA/ASME/SAE/ASEE Joint Propulsion Conference & Exhibit; American Institute of Aeronautics and Astronautics, 2002.
- (4) Cooper, M.; Shepherd, J. E. *Thermal and Catalytic Cracking of JP-10 for Pulse Detonation Engine Applications*, California Institute of Technology: Pasadena, CA, 2002.
- (5) Osmont, A.; Gökalp, I.; Catoire, L. Evaluating Missile Fuels. *Propellants, Explos., Pyrotech.* **2006**, *31*, 343–354.
- (6) Colket, M. B.; Spadaccini, L. J. Scramjet Fuels Autoignition Study. *J. Propul. Power* **2001**, *17*, 315–323.
- (7) Gao, C. W.; Vandeputte, A. G.; Yee, N. W.; Green, W. H.; Bonomi, R. E.; Magoon, G. R.; Wong, H.-W.; Oluwole, O. O.; Lewis, D. K.; Vandewiele, N. M.; Van Geem, K. M. JP-10 Combustion Studied with Shock Tube Experiments and Modeled with Automatic Reaction Mechanism Generation. *Combust. Flame* **2015**, *162*, 3115–3129.
- (8) Park, S. H.; Kwon, C. H.; Kim, J.; Han, J. S.; Jeong, B. H.; Han, H.; Kim, S. H. Mechanistic Insights into Oxidative Decomposition of exo-Tetrahydrodicyclopentadiene. *J. Phys. Chem. C* **2013**, *117*, 15933–15939.
- (9) Herbinet, O.; Sirjean, B.; Bounaceur, R.; Fournet, R.; Battin-Leclerc, F.; Scacchi, G.; Marquaire, P.-M. Primary Mechanism of the Thermal Decomposition of Tricyclodecane. *J. Phys. Chem. A* **2006**, *110*, 11298–11314.
- (10) Park, S. H.; Kwon, C. H.; Kim, J.; Chun, B.-H.; Kang, J. W.; Han, J. S.; Jeong, B. H.; Kim, S. H. Thermal Stability and Isomerization Mechanism of exo-Tetrahydrodicyclopentadiene: Experimental Study and Molecular Modeling. *Ind. Eng. Chem. Res.* **2010**, *49*, 8319–8324.
- (11) Xing, Y.; Fang, W.; Xie, W.; Guo, Y.; Lin, R. Thermal Cracking of JP-10 under Pressure. *Ind. Eng. Chem. Res.* **2008**, *47*, 10034–10040.
- (12) Morozov, A. N.; Mebel, A. M.; Kaiser, R. I. A Theoretical Study of Pyrolysis of exo-Tetrahydrodicyclopentadiene and Its Primary and Secondary Unimolecular Decomposition Products. *J. Phys. Chem. A* **2018**, *122*, 4920–4934.
- (13) Rao, P. N.; Kunzru, D. Thermal cracking of JP-10: Kinetics and product distribution. *J. Anal. Appl. Pyrolysis* **2006**, *76*, 154–160.
- (14) Zhao, L.; Chen, W.; Su, H.; Yang, J.; Kaiser, R. I. A Vacuum Ultraviolet Photoionization Study on Oxidation of JP-10 (exo-Tetrahydrodicyclopentadiene). *Chem. Phys. Lett.* **2020**, *754*, No. 137490.
- (15) Zhao, L.; Yang, T.; Kaiser, R. I.; Troy, T. P.; Xu, B.; Ahmed, M.; Alarcon, J.; Belisario-Lara, D.; Mebel, A. M.; Zhang, Y.; et al. A Vacuum Ultraviolet Photoionization Study on High-Temperature Decomposition of JP-10 (Exo-Tetrahydrodicyclopentadiene). *Phys. Chem. Chem. Phys.* **2017**, *19*, 15780–15807.
- (16) Zettervall, N. Reduced Chemical Kinetic Reaction Mechanism for JP-10-Air Combustion. *Energy Fuels* **2020**, *34*, 16624–16635.
- (17) Vandewiele, N. M.; Magoon, G. R.; Van Geem, K. M.; Reyniers, M.-F.; Green, W. H.; Marin, G. B. Experimental and Modeling Study on the Thermal Decomposition of Jet Propellant-10. *Energy Fuels* **2014**, *28*, 4976–4985.
- (18) Yetter, R. A.; Risha, G. A.; Son, S. F. Metal Particle Combustion and Nanotechnology. *Proc. Combust. Inst.* **2009**, *32*, 1819–1838.
- (19) Dreizin, E. L. Metal-based reactive nanomaterials. *Prog. Energy Combust. Sci.* **2009**, *35*, 141–167.
- (20) Javed, I.; Baek, S. W.; Waheed, K. Autoignition and Combustion Characteristics of Heptane Droplets with the Addition

of Aluminium Nanoparticles at Elevated Temperatures. *Combust. Flame* **2015**, *162*, 191–206.

(21) Jing, Q.; Wang, D.; Shi, C. Effects of Aluminum Powder Additives on Deflagration and Detonation Performance of JP-10/DEE Mixed Fuel under Weak and Strong Ignition Conditions. *Appl. Energy* **2023**, *331*, No. 120477.

(22) Luo, Y.; Xu, X.; Zou, J.-J.; Zhang, X. Combustion of JP-10-Based Slurry with Nanosized Aluminum Additives. *J. Propul. Power* **2016**, *32*, 1167–1177.

(23) Liu, L.; Zhang, Q.; Shen, S.; Li, D.; Lian, Z.; Wang, Y. Evaluation of Detonation Characteristics of Aluminum/JP-10/Air Mixtures at Stoichiometric Concentrations. *Fuel* **2016**, *169*, 41–49.

(24) Liu, J. Z.; Chen, B. H.; Wu, T. T.; Yang, W. J.; Zhou, J. H. Ignition and Combustion Characteristics and Agglomerate Evolution Mechanism of Aluminum in nAl/JP-10 Nanofluid Fuel. *J. Therm. Anal. Calorim.* **2019**, *137*, 1369–1379.

(25) Chen, B. H.; Liu, J. Z.; Li, H. P.; Yang, W. J.; Cen, K. F. Laser Ignition and Combustion Characteristics of Al/JP-10 Nanofluid Droplet. *J. Therm. Anal. Calorim.* **2019**, *135*, 925–934.

(26) E, X.-T.-F.; Zhang, L.; Wang, F.; Zhang, X.; Zou, J.-J. Synthesis of Aluminum Nanoparticles as Additive to Enhance Ignition and Combustion of High Energy Density Fuels. *Front. Chem. Sci. Eng.* **2018**, *12*, 358–366.

(27) E, X.-T.-F.; Pan, L.; Wang, F.; Wang, L.; Zhang, X.; Zou, J.-J. Al-Nanoparticle-Containing Nanofluid Fuel: Synthesis, Stability, Properties, and Propulsion Performance. *Ind. Eng. Chem. Res.* **2016**, *55*, 2738–2745.

(28) Allen, C.; Mittal, G.; Sung, C.-J.; Toulson, E.; Lee, T. An Aerosol Rapid Compression Machine for Studying Energetic-Nanoparticle-Enhanced Combustion Of Liquid Fuels. *Proc. Combust. Inst.* **2011**, *33*, 3367–3374.

(29) Brotton, S. J.; Malek, M. J.; Anderson, S. L.; Kaiser, R. I. Effects of Acetonitrile-Assisted Ball-Milled Aluminum Nanoparticles on The Ignition of Acoustically Levitated Exo-Tetrahydrodicyclopentadiene (JP-10) Droplets. *Chem. Phys. Lett.* **2020**, *754*, No. 137679.

(30) Lucas, M.; Brotton, S. J.; Min, A.; Woodruff, C.; Pantoya, M. L.; Kaiser, R. I. Effects of Size and Prestressing of Aluminum Particles on the Oxidation of Levitated exo-Tetrahydrodicyclopentadiene Droplets. *J. Phys. Chem. A* **2020**, *124*, 1489–1507.

(31) Lucas, M.; Brotton, S. J.; Min, A.; Pantoya, M. L.; Kaiser, R. I. Oxidation of Levitated exo-Tetrahydrodicyclopentadiene Droplets Doped with Aluminum Nanoparticles. *J. Phys. Chem. Lett.* **2019**, *10*, 5756–5763.

(32) Jin, Y.; Dou, S.; Yang, Q.; Xu, X.; Fu, Q.; Pan, L. Performance Characteristics of a Scramjet Engine Using JP-10 Fuel Containing Aluminum Nanoparticles. *Acta Astronaut.* **2021**, *185*, 70–77.

(33) He, C.; Kaiser, R. I.; Lu, W.; Ahmed, M.; Krasnoukhov, V. S.; Pivovarov, P. S.; Zagidullin, M. V.; Azyazov, V. N.; Morozov, A. N.; Mebel, A. M. Unconventional Gas-Phase Preparation of the Prototype Polycyclic Aromatic Hydrocarbon Naphthalene (C<sub>10</sub>H<sub>8</sub>) via the Reaction of Benzyl (C<sub>7</sub>H<sub>7</sub>) and Propargyl (C<sub>3</sub>H<sub>3</sub>) Radicals Coupled with Hydrogen-Atom Assisted Isomerization. *Chem. Sci.* **2023**, *14*, 5369–5378.

(34) He, C.; Kaiser, R. I.; Lu, W.; Ahmed, M.; Reyes, Y.; Wnuk, S. F.; Mebel, A. M. Exotic Reaction Dynamics in the Gas-Phase Preparation of Anthracene (C<sub>14</sub>H<sub>10</sub>) via Spiroaromatic Radical Transients in the Indenyl–Cyclopentadienyl Radical–Radical Reaction. *J. Am. Chem. Soc.* **2023**, *145*, 3084–3091.

(35) Kaiser, R. I.; Maksyutenko, P.; Ennis, C.; Zhang, F.; Gu, X.; Krishtal, S. P.; Mebel, A. M.; Kostko, O.; Ahmed, M. Untangling the Chemical Evolution of Titan's Atmosphere and Surface—from Homogeneous to Heterogeneous Chemistry. *Faraday Discuss.* **2010**, *147*, 429–478.

(36) National Synchrotron Radiation Laboratory. Photonization Cross Section Database. <http://flame.nslr.ustc.edu.cn/database>. (accessed August 8, 2023).

(37) Kaiser, R. I.; Zhao, L.; Lu, W.; Ahmed, M.; Krasnoukhov, V. S.; Azyazov, V. N.; Mebel, A. M. Unconventional Excited-State Dynamics

in the Concerted Benzyl (C<sub>7</sub>H<sub>7</sub>) Radical Self-Reaction to Anthracene (C<sub>14</sub>H<sub>10</sub>). *Nat. Commun.* **2022**, *13*, No. 786.

(38) Zhang, T.; Tang, X. N.; Lau, K. C.; Ng, C. Y.; Nicolas, C.; Peterka, D. S.; Ahmed, M.; Morton, M. L.; Ruscic, B.; Yang, R.; et al. Direct Identification of Propargyl Radical in Combustion Flames by Vacuum Ultraviolet Photoionization Mass Spectrometry. *J. Chem. Phys.* **2006**, *124*, No. 074302.

(39) Huang, C.; Wei, L.; Yang, B.; Wang, J.; Li, Y.; Sheng, L.; Zhang, Y.; Qi, F. Lean Premixed Gasoline/Oxygen Flame Studied with Tunable Synchrotron Vacuum UV Photoionization. *Energy Fuels* **2006**, *20*, 1505–1513.

(40) Meloni, G.; Selby, T. M.; Goulay, F.; Leone, S. R.; Osborn, D. L.; Taatjes, C. A. Photoionization of 1-Alkenylperoxy and Alkylperoxy Radicals and a General Rule for the Stability of Their Cations. *J. Am. Chem. Soc.* **2007**, *129*, 14019–14025.

(41) Savee, J. D.; Sztáray, B.; Welz, O.; Taatjes, C. A.; Osborn, D. L. Valence Photoionization and Autoionization of the Formyl Radical. *J. Phys. Chem. A* **2021**, *125*, 3874–3884.

(42) Qi, F. E. I.; McLroy, A. Identifying Combustion Intermediates via Tunable Vacuum Ultraviolet Photoionization Mass Spectrometry. *Combust. Sci. Technol.* **2005**, *177*, 2021–2037.

(43) Parker, D. S. N.; Kaiser, R. I.; Troy, T. P.; Kostko, O.; Ahmed, M.; Mebel, A. M. Toward the Oxidation of the Phenyl Radical and Prevention of PAH Formation in Combustion Systems. *J. Phys. Chem. A* **2015**, *119*, 7145–7154.

(44) Wu, X.; Zhou, X.; Hemberger, P.; Bodi, A. The Ionization Energy of The Vinyl Radical: A Mexican Standoff with a Happy Ending. *Phys. Chem. Chem. Phys.* **2019**, *21*, 22238–22247.

(45) Prendergast, M. B.; Kirk, B. B.; Savee, J. D.; Osborn, D. L.; Taatjes, C. A.; Hemberger, P.; Blanksby, S. J.; da Silva, G.; Trevitt, A. J. Product Detection Study of the Gas-Phase Oxidation of Methylphenyl Radicals Using Synchrotron Photoionisation Mass Spectrometry. *Phys. Chem. Chem. Phys.* **2019**, *21*, 17939–17949.

(46) Biswas, S.; Paul, D.; He, C.; Dias, N.; Ahmed, M.; Pantoya, M. L.; Kaiser, R. I. Counterintuitive Catalytic Reactivity of the Aluminum Oxide “Passivation” Shell of Aluminum Nanoparticles Facilitating the Thermal Decomposition of exo-Tetrahydrodicyclopentadiene (JP-10). *J. Phys. Chem. Lett.* **2023**, *14*, 9341–9350.

(47) Hunter, E. P. L.; Lias, S. G. Evaluated Gas Phase Basicities and Proton Affinities of Molecules: An Update. *J. Phys. Chem. Ref. Data* **1998**, *27*, 413–656.

(48) Bouwman, J.; McCabe, M. N.; Shingledecker, C. N.; Wandishin, J.; Jarvis, V.; Reusch, E.; Hemberger, P.; Bodi, A. Five-membered Ring Compounds from the ortho-Benzynes + Methyl Radical Reaction Under Interstellar Conditions. *Nat. Astron.* **2023**, *7*, 423–430.

(49) Bieri, G.; Burger, F.; Heilbronner, E.; Maier, J. P. Valence Ionization Energies of Hydrocarbons. *Helv. Chim. Acta* **1977**, *60*, 2213–2233.

(50) Malek, M. I.; Wu, C.-C.; Walck, S. D.; Pantoya, M. L. Hydration of Alumina (Al<sub>2</sub>O<sub>3</sub>) toward Advancing Aluminum Particles for Energy Generation Applications. *Colloids Surf., A* **2022**, *652*, No. 129740.

(51) Padhye, R.; McCollum, J.; Korzeniewski, C.; Pantoya, M. L. Examining Hydroxyl–Alumina Bonding toward Aluminum Nanoparticle Reactivity. *J. Phys. Chem. C* **2015**, *119*, 26547–26553.

(52) Pantoya, M. L.; Dean, S. W. The Influence of Alumina Passivation on Nano-Al/Teflon Reactions. *Thermochim. Acta* **2009**, *493*, 109–110.

(53) Walzel, R. K.; Levitas, V. I.; Pantoya, M. L. Aluminum Particle Reactivity as a Function of Alumina Shell Structure: Amorphous versus Crystalline. *Powder Technol.* **2020**, *374*, 33–39.

(54) Miller, K. K.; Gottfried, J. L.; Walck, S. D.; Pantoya, M. L.; Wu, C.-C. Plasma Surface Treatment of Aluminum Nanoparticles for Energetic Material Applications. *Combust. Flame* **2019**, *206*, 211–213.

(55) Mench, M. M.; Kuo, K. K.; Yeh, C. L.; Lu, Y. C. Comparison of Thermal Behavior of Regular and Ultra-fine Aluminum Powders (Alex) Made from Plasma Explosion Process. *Combust. Sci. Technol.* **1998**, *135*, 269–292.

(56) Gesner, J.; Pantoya, M. L.; Levitas, V. I. Effect of Oxide Shell Growth on Nano-Aluminum Thermite Propagation Rates. *Combust. Flame* **2012**, *159*, 3448–3453.

(57) Kanhaiya, K.; Heinz, H. Adsorption and Diffusion of Oxygen on Pure and Partially Oxidized Metal Surfaces in Ultrahigh Resolution. *Nano Lett.* **2022**, *22*, 5392–5400.

(58) Hong, S.; van Duin, A. C. T. Molecular Dynamics Simulations of the Oxidation of Aluminum Nanoparticles using the ReaxFF Reactive Force Field. *J. Phys. Chem. C* **2015**, *119*, 17876–17886.

(59) Zhang, Y. R.; van Duin, A. C. T.; Luo, K. H. Investigation of Ethanol Oxidation over Aluminum Nanoparticle Using ReaxFF Molecular Dynamics Simulation. *Fuel* **2018**, *234*, 94–100.

(60) Förster, G. D.; Calvo, F. Influence of Oxidizing Conditions on the Condensation of Aluminum Oxide Nanoparticles: Insights from Atomistic Modeling. *Appl. Surf. Sci.* **2020**, *512*, No. 145440.

(61) Murshed, S. M. S. Simultaneous Measurement of Thermal Conductivity, Thermal Diffusivity, and Specific Heat of Nanofluids. *Heat Transfer Eng.* **2012**, *33*, 722–731.

(62) Levitas, V. I.; Pantoya, M. L.; Chauhan, G.; Rivero, I. Effect of the Alumina Shell on the Melting Temperature Depression for Aluminum Nanoparticles. *J. Phys. Chem. C* **2009**, *113*, 14088–14096.

(63) Levitas, V. I.; Asay, B. W.; Son, S. F.; Pantoya, M. Mechanochemical Mechanism for Fast Reaction of Metastable Intermolecular Composites Based on Dispersion of Liquid Metal. *J. Appl. Phys.* **2007**, *101*, No. 083524.

(64) Levitas, V. I.; Pantoya, M. L.; Dikici, B. Melt Dispersion versus Diffusive Oxidation Mechanism for Aluminum Nanoparticles: Critical Experiments and Controlling Parameters. *Appl. Phys. Lett.* **2008**, *92*, No. 011921.

(65) Patel, V. K.; Joshi, A.; Kumar, S.; Rathaur, A. S.; Katiyar, J. K. Molecular Combustion Properties of Nanoscale Aluminum and Its Energetic Composites: A Short Review. *ACS Omega* **2021**, *6*, 17–27.

(66) Wu, B.; Wu, F.; Wang, P.; He, A.; Wu, H. Ignition and Combustion of Hydrocarbon Fuels Enhanced by Aluminum Nanoparticle Additives: Insights from Reactive Molecular Dynamics Simulations. *J. Phys. Chem. C* **2021**, *125*, 11359–11368.